



AMERICAN UNIVERSITY OF BEIRUT

AN AORTIC ARCH FLOW LOOP FOR THE STUDY OF  
HEMODYNAMIC INDUCED ENDOTHELIAL CELL INJURY  
AND INFLAMMATION

by  
MHAMAD MAHDI ALLOUSH

A thesis  
submitted in partial fulfillment of the requirements  
for the degree of Master of Engineering  
to the Department of Mechanical Engineering  
of the Faculty of Engineering and Architecture  
at the American University of Beirut

Beirut, Lebanon  
September 2015

AMERICAN UNIVERSITY OF BEIRUT

AN AORTIC ARCH FLOW LOOP FOR THE STUDY OF  
HEMODYNAMIC INDUCED ENDOTHELIAL CELL INJURY  
AND INFLAMMATION

by  
MHAMAD MAHDI ALLOUSH


Approved by:

Dr. Ghanem Oweis, Associate Professor  
Department of Mechanical Engineering



Advisor

Dr. Fadl Moukalled, Professor  
Department of Mechanical Engineering



Member of Committee

Dr. Asad Zeidan, Assistant Professor  
Department of Physiology



Member of Committee

Date of thesis defense: September 7, 2015

# AMERICAN UNIVERSITY OF BEIRUT

## THESIS, DISSERTATION, PROJECT RELEASE FORM

Student Name: \_\_\_\_\_

Last

First

Middle

Master's Thesis

Master's Project

Doctoral Dissertation

I authorize the American University of Beirut to: (a) reproduce hard or electronic copies of my thesis, dissertation, or project; (b) include such copies in the archives and digital repositories of the University; and (c) make freely available such copies to third parties for research or educational purposes.

I authorize the American University of Beirut, **three years after the date of submitting my thesis, dissertation, or project**, to: (a) reproduce hard or electronic copies of it; (b) include such copies in the archives and digital repositories of the University; and (c) make freely available such copies to third parties for research or educational purposes.

---

Signature

Date



## ACKNOWLEDGMENTS

Special thanks are for Professor *Ghanem Oweis* who advised me throughout the Master's program, not only in the technical issues, but also in the moral ones. It's a great pleasure that he accept my sincere gratitude for his help and supervision.

My recognition and gratitude are addressed to those who helped in accomplishing the work – experimental fluids lab colleagues namely *Hussein Daoud*, lab managers and the shops' staff.

I shall also thank the collaborators from the physiology department, particularly Professor *Asaad Zeidan* and R.A. *Sarah Hanache*, who contributed significantly in the research.

# ABSTRACT

Mhamad Mahdi Alloush for Master of Engineering  
Major: Mechanical Engineering

Title: An Aortic Arch Flow Loop for the Study of Hemodynamic Induced Endothelial Cells Injury and Inflammation

Atherosclerosis is a major cardiovascular disease which develops on the interior wall of a blood artery particularly at locations where geometric features like bends exist. In this work, we present the design and implementation of an aortic arch model in a flow loop in order to simulate blood flow in aorta. The main objective is to investigate the characteristics of the flow in an aortic arch and figure out some significant hemodynamic flow quantities like wall shear stress. Refractive index matching PIV is used for the determination of velocity patterns in the model.

PIV have proved the presence of deceleration behavior of the flow in the near-inner wall boundary, the fact that led to low shear stress magnitudes at these regions. While acceleration behavior of the flow have been proved on the near-outer wall boundary which led to higher shear stress levels than those at the inner boundary.

Endothelial cells were cultured on the lower and upper walls of the aortic lumen and the system was made to run under flow conditions. Signal identification and quantification tests have explored the occurrence of specific expressions of proteins, more prominent in the lower wall region. This finding explains the low shear stress levels obtained by PIV post-processing at the mentioned location. Given that, there exists a strong correlation between the hemodynamic forcing level of flow with Endothelial cell response and function.

# CONTENTS

ACKNOWLEDGMENTS .....	v
ABSTRACT .....	vi
LIST OF ILLUSTRATIONS .....	ix

## Chapter

<b>I. INTRODUCTION.....</b>	<b>1</b>
A. Atherosclerosis and Hemodynamics .....	<b>1</b>
B. Oversimplified Trials to Explain the Existing Correlation between Hemodynamics and Inflammation and Bridging the Gap.....	<b>2</b>
C. Essential Facts about Flows in Bends .....	<b>3</b>
D. Thesis Objectives.....	<b>4</b>
<b>II. DESIGN CONSIDERATIONS OF THE AORTIC FLOW LOOP .....</b>	<b>6</b>
A. The Aortic Arch Model .....	<b>6</b>
B. Circulating Pump, Pulse Dampeners, Transducers and Tubing.....	<b>10</b>
1. Circulating pump .....	<b>10</b>
2. Pulse Dampeners .....	<b>11</b>
3. Transducers.....	<b>13</b>
4. Tubing and Couplings .....	<b>14</b>
C. Working Fluid.....	<b>16</b>

III. FLOW VISUALIZATION BY PIV .....	20
IV. PULSE DAMPENERS' EFFECTIVENESS.....	28
V. RESULTS.....	34
VI. BIOLOGICAL INVESTIGATIONS.....	46
VII. DISCUSSION .....	52
VIII. CONCLUSION .....	58
REFERENCES .....	60

# ILLUSTRATIONS

Figure	Page
1. Aortic arch schematic - dimensions in mm .....	7
2. 3D model of the aortic arch representing the two complementary PDMS pieces ...	7
3. Figure 3 - (a) PDMS aortic model parts 1 & 2 (b) Aortic model fitted in a Plexiglas box.....	9
4. Actual aortic model's dimensions .....	9
5. 3-roller head peristaltic pump .....	11
6. (a) Schematic of the pulse dampener design. Pulsatile liquid flow is introduced through the inlet on the side, where it flows upwards and then radially outwards through the narrow gap at the top to slow down and laminarize; it then drains down the sidewalls of the pulse dampener to collect in the lower part and exit with minimal pulsatility from the bottom. (b) Picture of the implemented design (external retaining box removed) .....	13
7. <i>From left to right:</i> USB pressure transducer, magnetic flow meter, k-type thermocouple .....	14
8. (a) BioPharm Tubing (b) Quick disconnect couplings .....	15
9. Picture of the circulating flow loop connected to the aortic arch .....	16
10. (a) NaI solution (b) Pure water .....	19
11. Laser beam development through a set of cylindrical lenses into a laser sheet which cuts the aortic arch's half-plane (the plane passes through and parallel to the centerline) .....	22
12. A planform view of the lens setup showing the types of lenses and pointing out the process of rotating the laser sheet about the third lens (plano-concave) through displacing it vertically downwards .....	22
13. Laser sheet cuts the aorta's half-plane at its inlet .....	23
14. Camera's optical axis is set normal to the laser sheet.....	23

15.	Six fields of view are planned to cover the whole aortic arch.....	24
16.	Sample raw image of the inlet .....	24
17.	Sample raw images of (a) FOV1 and (b) FOV2.....	26
18.	Stitched FOV's .....	27
19.	Pressure signals.....	30
20.	Flow rate signals .....	31
21.	(a) Pressure dampening efficiency vs. time (b) Flow rate dampening efficiency vs. time.....	33
22.	PIV velocity field at FOV1 at 400 rpm.....	36
23.	Flow rate signal at 400 rpm .....	37
24.	Time-averaged velocity profiles at the inlet for the two pump speeds (a) 147 and (b) 400 rpm.....	38
25.	Time-averaged velocity magnitude fields and levels at FOV1 at (a) 147 and (b) 400 rpm. Levels are in mm/s .....	39
26.	Time-averaged velocity levels throughout the aortic arch at (a) 147 and (b) 400 rpm. Levels are in mm/s .....	40
27.	Time-averaged velocity fields and levels at FOV2 at (a) 147 and (b) 400 rpm. Levels are in mm/s.....	41
28.	A boundary region of the aortic arch showing sets of tangent vectors emerging from points on the boundary .....	43
29.	A schematic showing the arch within the polar coordinate system (O, $\theta$ ) .....	43
30.	Shear Stress vs. theta along inner and outer walls at (a) 147 rpm and (b) 400 rpm.....	44
31.	Microscopic imaging of EC growth on the lumen of the aortic model 24 hours after seeding and under static conditions (40X) .....	47
32.	Upper and lower regions on the lumen show different EC alignments .....	47
33.	Protein expression and phosphorylation at (a) 50 rpm and (b) 400 rpm .....	50

34.	Normalized protein quantities acquired from the lower region.....	51
35.	(a) A raw image of FOV1 that shows how the lower (outer-radius) boundary is curved (b) Illustration of the velocity profiles skewness due to the outer wall curvature starting prior to that of the inner wall .....	52
36.	Velocity Profile at a given cross section of FOV5. (a) Actual velocity Profile (b) Velocity profile with mean subtracted .....	54
37.	Velocity profiles at 400 rpm along a section of the aortic arch showing (a) actual velocity vectors and (b) modified velocity vectors by the subtraction of the local cross sectional mean of velocity .....	55
38.	Vorticity contour at (a) 147 rpm and (b) 400 rpm.....	56

# CHAPTER I

## INTRODUCTION

### **A. Atherosclerosis and Hemodynamics**

Cardiovascular disease CVD is the number one cause of death in the world population (1, 2) and was behind 1 of every 6 deaths in the United States in 2006 (3) with massive socio economic costs (4). Atherosclerotic CVD is the primary factor in these deaths (3). Atherosclerosis is defined as plaque formation at specific zones on the interior walls of blood vessels and may result in infraction or blockage of blood flow to vital organs such as the heart and the brain. The plaque buildup is thought to occur in response to inflammation of the blood vessel (5, 6). Recent studies have produced convincing evidence linking inflammation of the blood vessel to hemodynamic and mechanical factors such as flow turbulence, wall shear stress, static pressure, and vessel stretching (7, 8 and 9). The prevailing locations for atherosclerotic plaque formation correlate well with geometric blood vessel features such as bifurcation, side branching, and arterial curvature which are known to give rise to flow separation and disturbed or low wall shear stress levels (10). The wall shear stress acts on a monolayer of cells lining the lumen of blood vessels in the cardiovascular system known as endothelial cells EC. These cells are in direct contact with blood flow, and it is these cells that provide the primary linkage between blood vessel inflammation and hemodynamic forcing such as the viscous shear. EC sense the hemodynamic shear stress and respond accordingly whether in health or disease through different biological pathways in a complex process known as mechanotransduction (11,



12). For instance, changes in the shear stress level can induce changes in the amounts of secretion of certain biochemical molecules from EC that alter its function and can eventually lead to remodeling of the blood vessel structure such as dilatation and constriction (12). These changes can be temporary or chronic.

### **B. Oversimplified Trials to Explain the Existing Correlation between Hemodynamics and Inflammation and Bridging the Gap**

In-vitro investigations have been essential in the understanding of cardiovascular disease through identifying certain mechano-transduction pathways in health and disease states. They are advantageous as they provide the ability to individually isolate and study cardiovascular factors by minimizing interferences from many other complicating factors present in vivo. In vitro inflammation studies of the cardiovascular system have probed a large number of possible disease-affecting factors such as hypertensive pressure, pulsatile pressure, mechanical stretch, temperature, oxygen level, and nutrient supply (13).

Laboratory studies on the role of hemodynamic forces in altering EC function and bio-chemical signaling have been conducted on excised blood vessels ex-vivo; or in-vitro using EC culture in unrealistically simplified flow conditions. The first approach utilizes realistic vessel geometry but suffers from a lack of knowledge of the underlying flow details within the vessel and is generally limited to knowledge of the bulk flow rate. The second approach boasts of detailed knowledge of the flow forcing but suffers from unrealistically over-simplified flow geometry such as a petri dish. There is a gap between the two approaches that requires bridging to permit the study of EC signaling and response to well-characterized flow conditions, in realistic vessel geometries. The current work is

aimed at narrowing this gap by introducing anatomically relevant in-vitro blood vessel geometry where the hemodynamic flow can be characterized in detail. The in-vitro flow model is constructed to allow EC culture on the lumen of the blood vessel besides bio analysis. The geometry under consideration in this work is a 180 deg. arterial bend typical of a human aortic arch. The vessel is connected to a circulating flow loop where arterial flow parameters can be monitored and controlled. The aortic bend geometry is chosen because of its known association with EC inflammatory response and plaque formation (10, 12). Particle image velocimetry PIV will be used to measure the flow patterns at the half-plane to identify regions of flow separation and low wall shear stress levels; and regions of healthy levels of shear stress. This level of flow details is necessary to be able to correlate the bend hemodynamics to the function and signaling of EC grown on various parts of the lumen. In the following we discuss the in-vitro flow loop model and the flow measurement scheme with attention to the implementation of refractive index matching PIV, which is a technique used to eliminate optical distortions in the illumination and the imaging paths within the flow visualization process due to the curved vessel interface of the aortic model.

### **C. Essential Facts about Flows in Bends**

Moreover, the fluid dynamics in a curved vessel exhibit various localized flow features such as flow deceleration, separation, and reversal on the inner bend wall; a consequence of this flow behavior is low wall shear stresses. On another hand, flow acceleration on the outer wall of the bend is experienced and hence high wall shear stresses are expected. It's worth mentioning that 3D flow structures and counter rotating Dean's vortices (14, 15) are major characteristics of a flow in curved channel. Dean's vortices are

defined as a pair of counter-rotating vortex cells that are produced as centrifugal and viscous forces interact (16). This hypothesis first made by Dean was based on mathematical analysis and later observed experimentally by Eustice (17); the experimental observations have depicted counter-rotating vortices in the plane perpendicular to the center line of the pipe. However, no regard to the Dean's vortices is given in the scope of this work because the concern is only limited to the half-plane which is the plane parallel to the centerline. In specific, calculations of shear stress require that the near-wall region be sufficiently characterized, so this task is not related to the 3D effects which dominate in the far-from-region.

#### **D. Thesis Objectives**

The objectives of this study are:

1. Design and build an in-vitro setup consisting of an aortic arch model with typical dimensions and a flow loop taking into consideration good sterility of the environment. It's also required that the aortic model be optically accessible to allow quantitative flow visualization (particle image velocimetry, PIV) and hemodynamic flow properties estimation. The latter requirement shall be fulfilled by implementing the aqueous solution which has a matched refraction index with the aorta model's material. Physical accessibility to the aortic lumen is required as well to permit cell culturing and growth under flow conditions
2. Design and implement pressure pulse dampeners that reduce significant pulsations in the flow and also implement air bubble trappers to prevent air bubbles from

flowing towards the aorta model as these may cause injury to the cell culture as well as optical distortions to the flow visualization procedure

3. Do cinema PIV for the whole aortic arch at the half-plane which contains the arch's centerline where 3D structures are thought to be minimal. Then, generate based on PIV velocity fields wall shear stress levels throughout the inner and outer boundaries of the aortic arch. The system is to operate at speed modes, low and high speeds. These modes are said to be mimicking two states of a human being, the rest and exercise states. Reynolds number matching is an important issue; Reynolds number should be on the same order of the real Reynolds number of the two human being states
4. Endothelial cells are to be seeded and cultured on the wall of the arterial lumen. The cells' response under flow conditions is to be explored. Protein signaling is the biological process to be manipulated to identify and quantify the present proteins in the vicinity of the cells from the lower and upper walls. Shear stress results are to be evaluated in the light of biological findings to prove the linkage of the hemodynamic shear stress to the cell response and function.

## CHAPTER II

### DESIGN CONSIDERATIONS OF THE AORTIC FLOW LOOP

#### A. The Aortic Arch Model

The aortic arch was cast from liquid silicone polydimethylsiloxane PDMS that cured at room temperature overnight. The PDMS used for the aorta cast has very good cell adhesion qualities and it is optically clear for flow visualization and imaging. The curved vessel had a design round cross section of 14.3 mm ID nominal, and a bend curvature of 35 mm. The terms *Inner Boundary* and *Outer Boundary* will be used frequently in the text; the first refers to the smaller-radius aortic wall while the second refers to the larger radius aortic wall. The bend lied in a plane with the inlet and outlet separated by 180°. These dimensions were derived from typical physiological values (18, 19). The model was manufactured in two parts to provide physical access to the arch's lumen for EC culture and sampling. A schematic of the aortic arch and a 3D drawing are shown in Figures 1 and 2. Prior to casting, micro glass beads were sprinkled on the PDMS liquid. The liquid was stirred after that to have the beads spread evenly. These beads are used as guides in the imaging procedure later; the issue will be discussed in more details in a separate context.

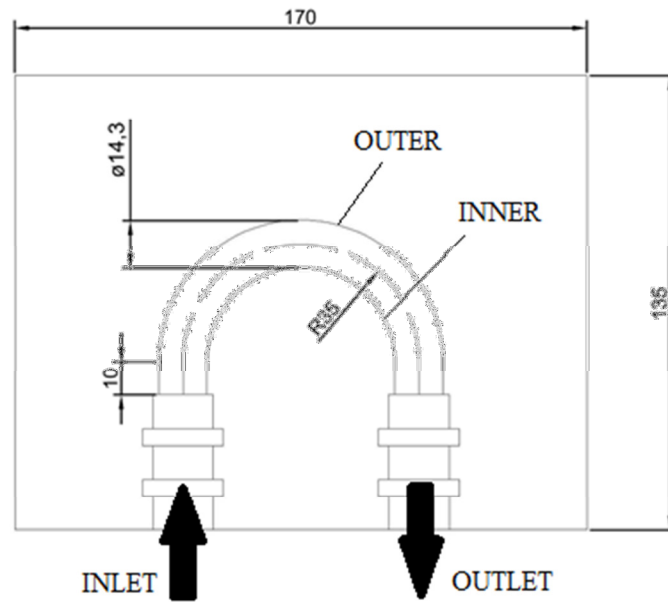


Figure 1 - Aortic arch schematic - dimensions in mm

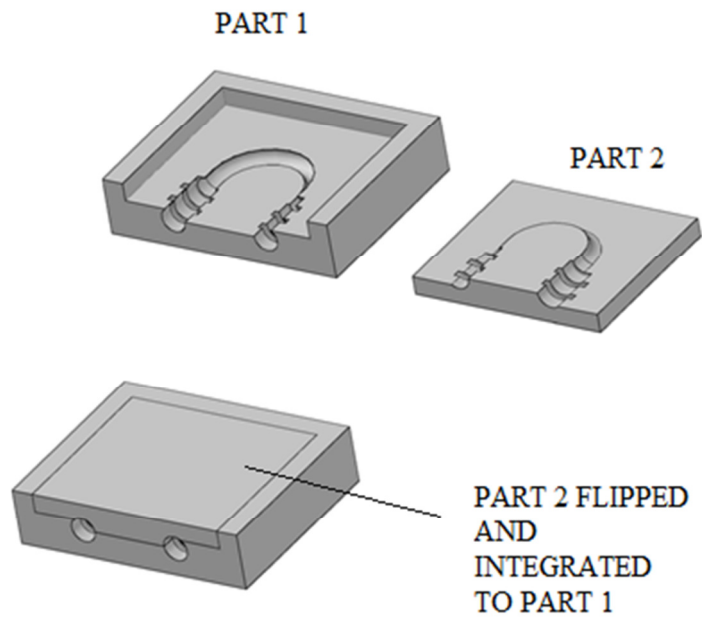
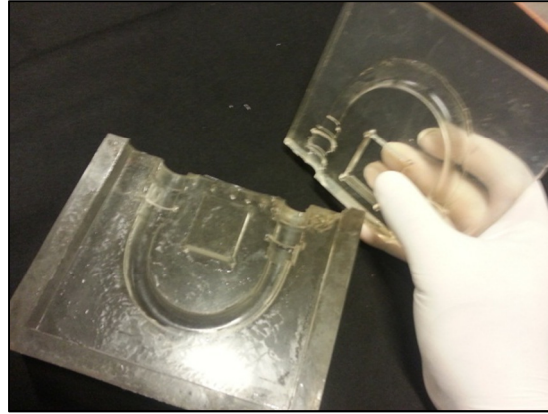
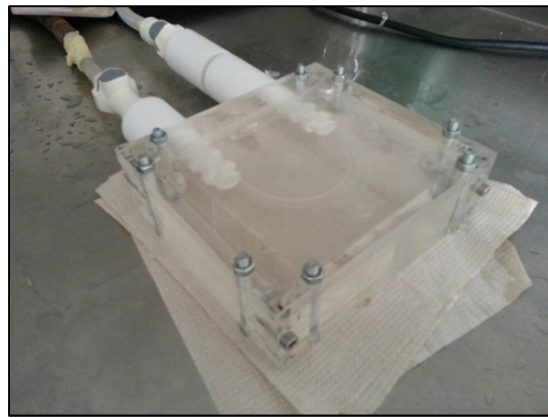


Figure 2 - 3D drawing of the aortic arch representing the two complementary PDMS pieces

Picture of the manufactured aortic arch model is presented in **Figure 3-a**. **Figure 3-b** presents the model fitted in a Plexiglas box used initially as the PDMS cast liquid container and later on used as a tightening cover. Appearing also in **Figure 3-b**, 2 Teflon-made fittings (white colored pieces) at the inlet and outlet of the aortic model. These fittings connect the model to the setup described in the next sections. The actual model's dimensions after casting were measured to be a bit deviated due to molds' tolerances and casting process imperfections; **Figure 4** shows a schematic of the actual model based on measured dimensions. The actual nominal diameter of the aortic arch is  $13.5\text{ mm}$  as shown in **Figure 4** while the radius of curvature of the arch is found to be  $33\text{ mm}$ . The fitting at the inlet side includes a development length piece. It is a straight pipe of length  $L$  and diameter  $D$  – the same diameter as the aortic arch (ID  $14.3\text{ mm}$ ) – and is flush mounted with it. It contains an upstream flow straightener section formed of  $>80$  small stainless pipes  $1.27\text{ mm}$  ID, and  $20\text{ mm}$  long. They act to streamline the flow, set it unidirectional, and break up any large-scale vortical structures. The length ratio  $L/D > 10$  provides a stretch of pipe for the flow to sufficiently develop prior to entering the aorta.



(a)



(b)

Figure 3 - (a) PDMS aortic model parts 1 & 2 (b) Aortic model fitted in a Plexiglas box

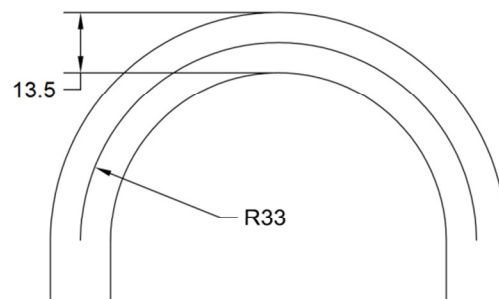


Figure 4 - Actual aortic model's dimensions



## **B. Circulating Pump, Pulse Dampeners, Transducers and Tubing**

### ***1. Circulating pump***

The aortic arch was connected through fittings to a circulatory flow loop driven by a 3-roller peristaltic pump (Model FH100x, Thermo scientific, USA) to maintain sterile conditions for cell proliferation. See **Figure 5**. A peristaltic pump may be used to benefit of its sterility option rather than establishing a pulsatile flow. In fact, certain studies may require steady flows to isolate the effects of pulsatility from other experimental variables. Also, in rigid vessel investigations, as is the case in certain types of cardiovascular disease and/or in old age (20), it may be sufficient to work with non-pulsatile flows. A number of experimental studies have implemented non-pulsatile flow (21-22-23). It's important to state at this point that pulsatility could be a source of noise and/or harm to the system so some sort of pulse dampeners are to be implemented. The issue of pulse dampeners is discussed in the next section. Since it's required in this work to calculate the shear stress throughout the aortic arch, it's crucial to specify the controlling variables. In this work, as mentioned previously, the focus is on the influence of geometry on shear stress which is a major contributor to the so called mechano-transduction biological process; determining the variation of shear stress as a function of geometry is what this thesis pursues, thus, pulsatility is a sort of mislead. Moreover, it's stated in literature that shear stress slew rate, or time rate of change of shear stress has a significant impact on cell elongation and remodeling; this work includes cell culturing on the inner arterial wall for purposes discussed later.

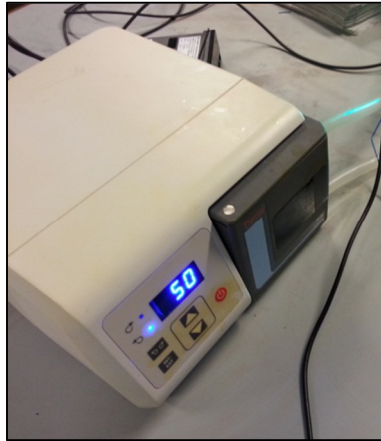


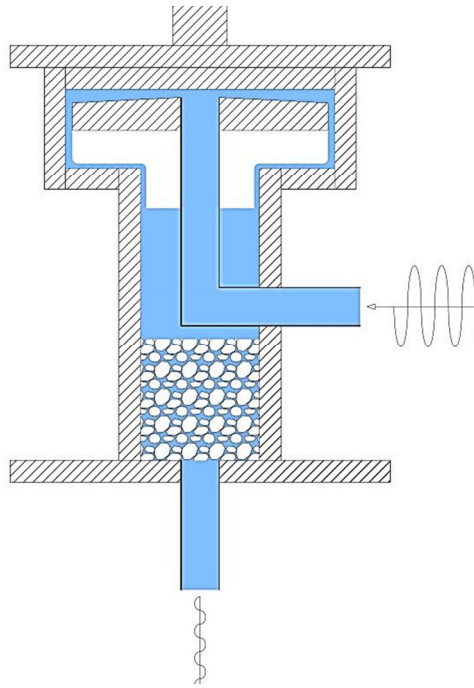
**Figure 5 - 3-roller head peristaltic pump**

## ***2. Pulse Dampeners***

The pump's inlet and outlet were connected to large-acoustic-impedance-mismatch pulsation dampeners consisting of a filled container with an air gap on top to minimize the propagation of the pump's pulsations to the aortic flow. The pulse dampener consisted of a cylindrical body half full of liquid, with its top volume containing air. The incoming liquid flowed through the center of an annular gap formed by two large discs at the top of the damper body, then radially outwards to the sidewalls at considerably reduced speed. **Figure 6** illustrates the construction of the pulse dampener. The liquid drained down smoothly on the sides of the container to collect at the bottom with minimal air entrapment and then exited the pulse dampener through a side opening near the bottom. A high porosity plastic sponge placed in the liquid at the bottom arrested any entrained bubbles and prevented them from flowing out of the pulse dampener. This element was critical for the biocompatible performance of the flow system as air bubbles can cause injury to the

vital cells. The whole dampener was fixed in a rectangular box for good bench-top stability.

Pulse dampener effectiveness is discussed later in a separate section.



(a)



(b)

**Figure 6 – (a) Schematic of the pulse dampener design. Pulsatile liquid flow is introduced through the inlet on the side, where it flows upwards and then radially outwards through the narrow gap at the top to slow down and laminarize; it then drains down the sidewalls of the pulse dampener to collect in the lower part and exit with minimal pulsatility from the bottom. (b) Picture of the implemented design (external retaining box removed)**

### **3. Transducers**

A +/- 2.5 psi gage pressure transducer (Model PX409, Omegadyne Inc., OH, USA) was installed on the outlet fitting with a 0.5 mm pressure port, and its output was written directly to file through a USB computer port. A magnetic flow meter (Model FMG9, Omega, Stanford, USA) was installed in the flow loop for independent flow monitoring downstream from the outlet section of the aortic arch. An independent screen for digital display of flow rate is supplied with the flow meter. The volume flow rate unit of preference to the author used to be LPM; the screen's settings were adjusted to depict LPM

units with sufficient precision. A 120 W electric heating band (Omegalux, USA) with a K-type thermocouple were used to monitor and control the temperature of the working fluid.

Pictures of the introduced transducers are presented in **Figure 7**.



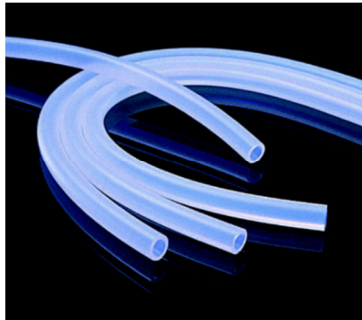
**Figure 7 - From left to right: USB pressure transducer, magnetic flow meter, k-type thermocouple**

#### ***4. Tubing and Couplings***

BioPharm Silicone tubing (Thermo Scientific, USA) was provided as means of connecting the components. The provided tubing possesses ultra-smooth inner surface, flexibility, translucency and excellent biocompatibility while it's odorless and nontoxic. Involved also are quick disconnect plastic valved couplings (CPC, USA) to provide easy and safe connect and release process of the tubing. See **Figure 8**.



(a)



(b)

**Figure 8 - (a) BioPharm Tubing (b) Quick disconnect couplings**

An overall picture of the flow loop system is shown in **Figure 9**. Assuming the peristaltic pump to be the starting reference point, the flow is pumped to the first pulse dampener and then passes to the development entrance section where it's expected to develop. It enters next to the aortic arch model and leaves from the outlet where the pressure transducer is mounted. Situated downstream the outlet, are the heating band, the magnetic flow meter, the k-type thermocouple and the second pulse dampener respectively.

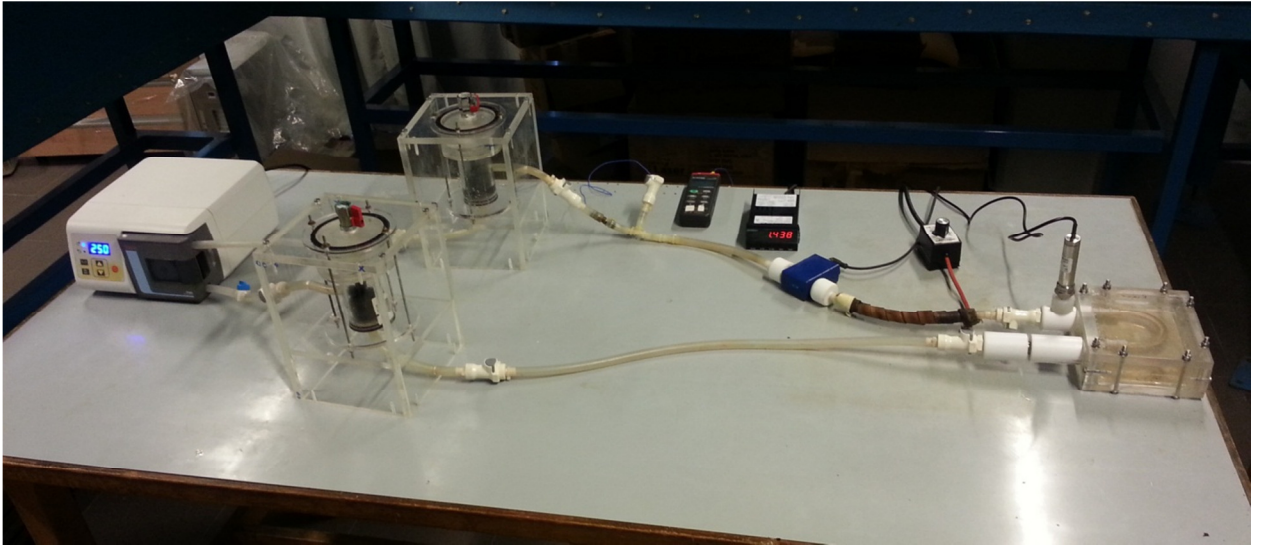


**Figure 9 – Picture of the circulating flow loop connected to the aortic arch**

### **C. Working Fluid**

Minimizing the total working fluid volume was an important consideration aiming at maximizing the biochemical signaling concentration detection sensitivity. It was found that the optimum amount of fluid to introduce into the system is that which leaves no air gaps in the loop and fill the pulse dampeners to just above the sponges. Adding more fluid has a drawback on the pulse dampener effectiveness because the latter is mainly dependent on the volume of air trapped in the upper space. Reducing the amount, as well, has a negative aspect at the sponge level such that air bubbles would have a higher tendency to escape from the sponge. This is because of the porous aspect of the sponge through which the flow passes in a turbulent fashion, the reason why air gets more entrained. To sum up, the optimum volume is measured to be approximately 600 ml.

The fluid should have a matched index of refraction with the PDMS; and it should have a biologically relevant kinematic viscosity ( $\nu = \frac{\mu}{\rho}$ ) to result in a matched range of

hemodynamic forcing, which requires matching the flow Reynolds number; or alternatively the Dean number that derives from it and used specifically for curved vessels. There are a number of alternatives that can be used to satisfy both requirements including aqueous solutions of sucrose, sodium chloride, sodium iodide, glycerol, or combinations thereof at various concentrations. These provide sufficient, simultaneous control over the index of refraction and the kinematic viscosity. The mechanical and biological measurements will be conducted separately and they are not to be performed simultaneously because the cells will block the optical path needed for flow visualization; while some of the aforementioned working fluids can be toxic to the cells and/or will produce un-intended biochemical stimulants.

The working fluid used for the flow visualization experiments reported later was an aqueous solution of NaI to closely match the index of refraction of the PDMS model,  $n = 1.43$ . A useful empirical formula of the refractive index of NaI (30) in terms of the concentration  $c$  of NaI is:

$$n = 0.2425c^2 + 0.09511c + 1.335$$

As stated by **Ref. 24**, refractive index of *NaI* is influenced by the solution's temperature as well as the illumination wavelength. However, the above formula is experimentally consistent with temperatures ranging between 20 °C and 40 °C at wavelength of 589 nm. The working temperature of the solution was elevated to 35 °C as this temperature is convenient to achieve a better solubility; solubility generally increases with increased temperature while this is appreciable to keep the solution away of crystallization. The flow visualization process, discussed later, includes illuminations of wavelengths



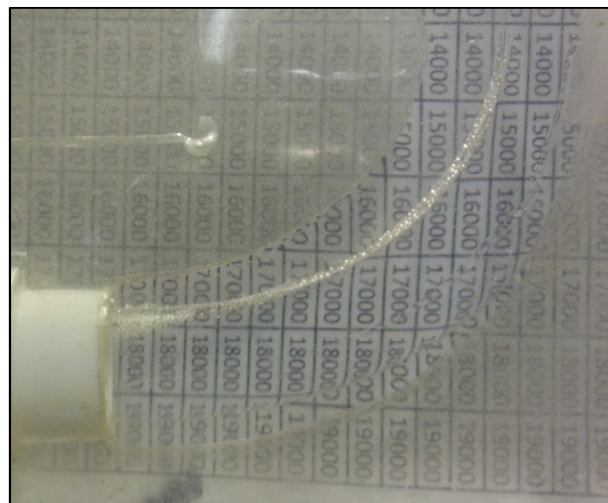
ranging between 457-512 nm which are quite coherent with the order of magnitude of that used in Ref. 24.

Then, to get a refractive index of 1.43, NaI concentration must be 42.77% according to the stated empirical formula. Physical properties of NaI solution with the specified concentration and temperature (25) are found to be:

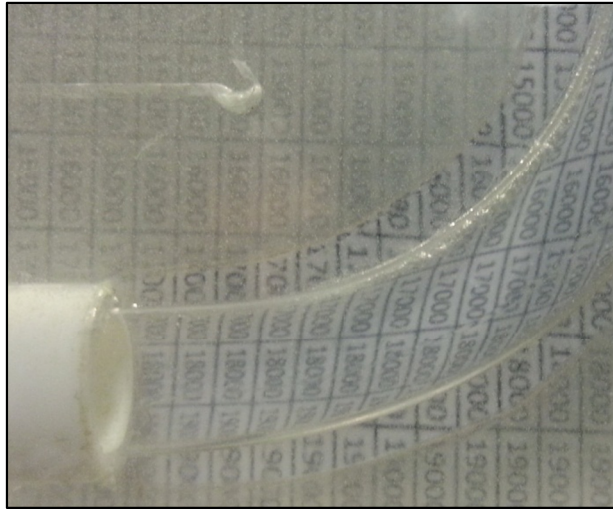
$$\mu = 0.00116 \text{ Pa}\cdot\text{s}$$

$$\rho = 1466.7 \text{ kg/m}^3$$

To demonstrate how the optical-matching working fluid (NaI solution) significantly minimizes distortions that would naturally be observed with water, images in **Figure 10a and 10b** show a printed table placed behind the aorta model filled with the optically-matched working fluid and pure water respectively.



(a)



(b)

Figure 10 – (a) NaI solution (b) Pure water

## CHAPTER III

### FLOW VISUALIZATION BY PIV

PIV is the primary flow measurement tool used in this study to characterize the hemodynamic forcing in the aortic arch. PIV works by seeding tracer particles into the flow and illuminating a 2-D planar area in the flow with a laser sheet. The seeded particles will appear as bright points in an otherwise dark background. A camera is used to take time-lapsed images of the flow tracers as they move with the flow. A cross correlation algorithm analyzes consecutive image pairs and produces 2-D maps of the tracer particle displacements and velocities at that instant of time. Further analysis of the velocity fields can provide quantitative hemodynamic flow properties, with the most important being the shear stress; which is the friction force exerted by the blood flow on the wall. Additionally, PIV can provide information on the level of flow disturbance and turbulence in different parts of the aortic arch, and it can provide evidence on the locations of flow separation and low shear stress, often associated with vessel disease. These are all critical factors affecting endothelial cell health and function.

In specific, the PIV system consisted of a 3W Argon ion laser source for illumination (Reliant 1000m, Laser Physics, UK) and a Phantom V9.0 CCD camera (Vision Research, USA) for imaging. The system was operated in cinematic imaging mode to produce time resolved PIV measurements at frame rates up to  $1200 \text{ s}^{-1}$ . The flow was seeded with  $<5 \text{ }\mu\text{m}$  glass beads of specific gravity 1.05. The laser beam was expanded in one direction and thinned in the other direction into a narrow light sheet using cylindrical

lenses as shown in **Figure 11**. The first inline lens is a bi-convex lens of focal distance  $f = 68.17 \text{ mm}$ . The laser beam emerges from the laser with a nominal diameter  $> 1 \text{ mm}$  and converges transversely to a finer diameter as it crosses the bi-convex lens. At the focal point, a plano-convex lens is placed to preserve the fine diameter of the beam as the beam would diverge afterwards. Beyond the second lens, a plano-concave lens is placed 12.7 cm ahead to enforce the beam to diverge laterally and establish a laser sheet that cuts the half-plane of the aortic arch. The arch is fixed 60 cm away of the third lens, a distance sufficient to cover a height of 4 cm at the rear side of the arch. The third lens is made moveable on a vertical handle; an action suitable for rotating the laser sheet with enough degrees to disclose all of the arch's pieces. This is sketched in **Figure 12**. A picture of the arch is presented in **Figure 13** where the laser sheet cuts the half-plane of the arch at its inlet side. The camera's optical axis was set normal to the light sheet (see **Figure 14**) and imaged a field of view of 22 mm by 30 mm. The camera was successively moved to result in six overlapping fields of view covering the whole aortic arch geometry; this is sketched in **Figure 15**. A sample raw image of FOV1 as captured by the Phantom camera is shown in **Figure 16**. Tracer particles differ in size as can be seen in the raw image. This is due to the finite-thickness aspect of the laser light sheet. Appearing also in the picture are tracer particles in the region outside the aortic arch. As introduced before, these particles shall be used as means of matching criteria of the different aortic sections with each other, a process which will be called *Stitching*.

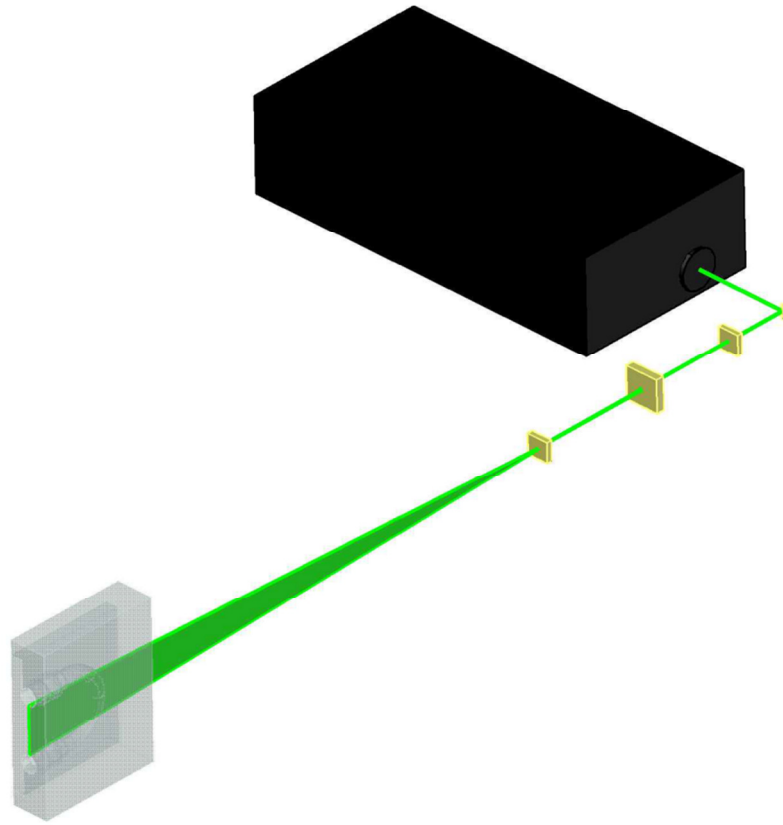


**Figure 11 - Laser beam development through a set of cylindrical lenses into a laser sheet which cuts the aortic arch's half-plane (the plane passes through and parallel to the centerline)**

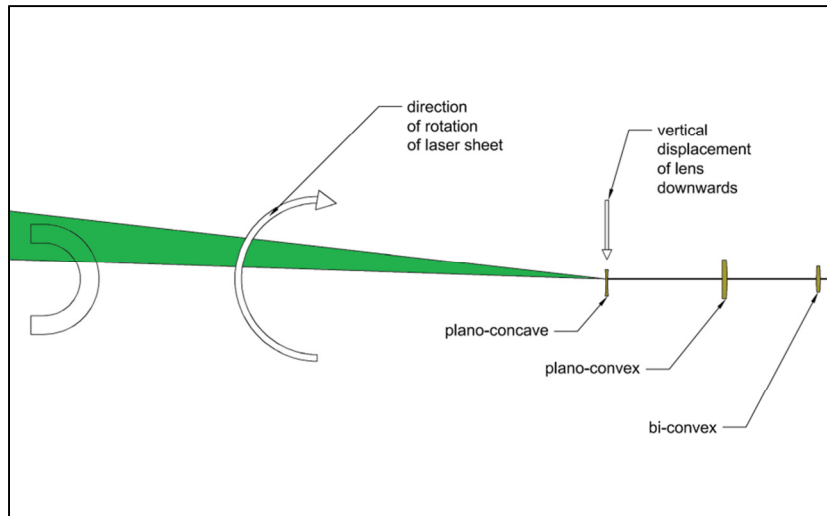


**Figure 12 - A planform view of the lens setup showing the types of lenses and pointing out the process of rotating the laser sheet about the third lens (plano-concave) through displacing it vertically downwards**

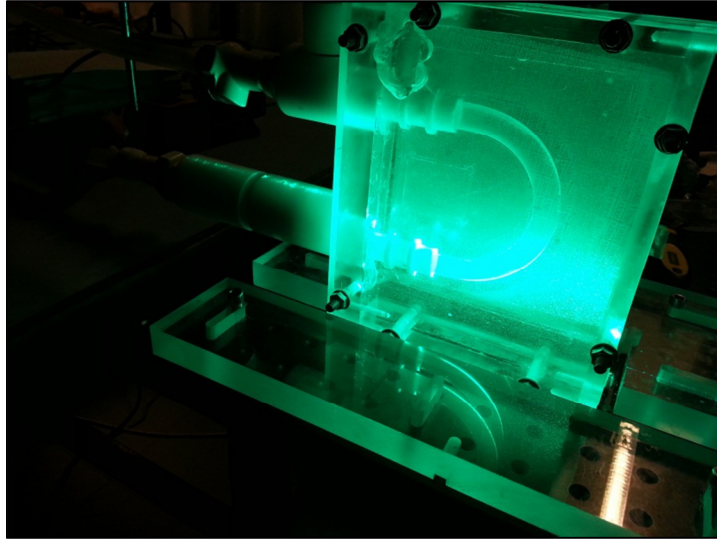


**Figure 13 - Laser sheet cuts the aorta's half-plane at its inlet**

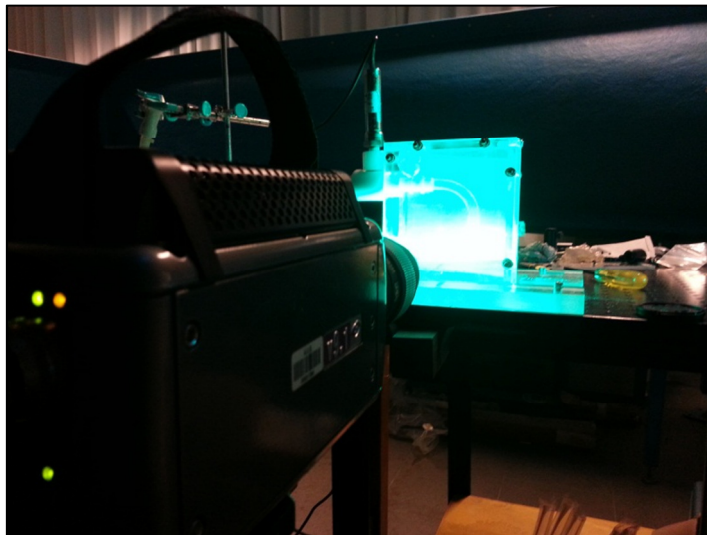


**Figure 14 – Camera's optical axis is set normal to the laser sheet**

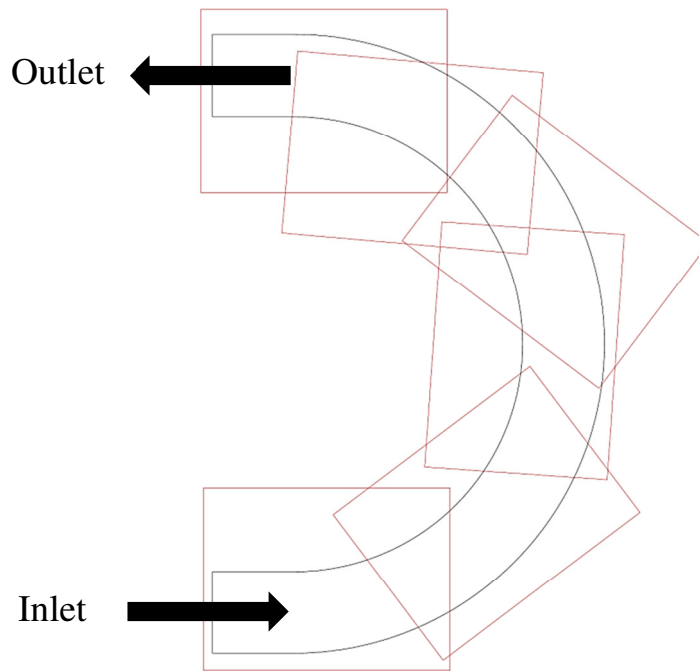


**Figure 15 - Six fields of view are planned to cover the whole aortic arch**

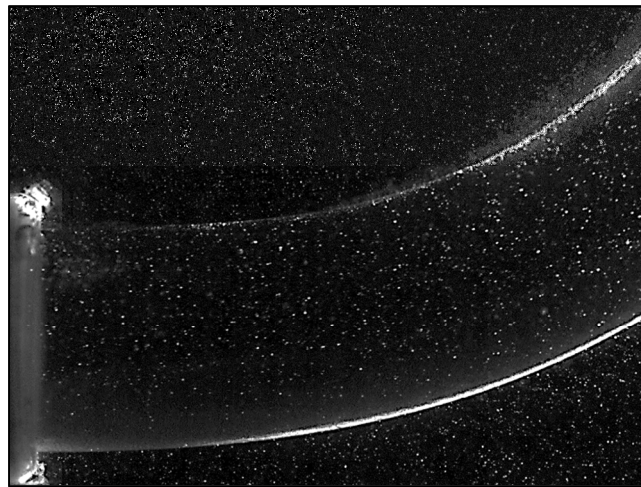


**Figure 16 - Sample raw image of the inlet**

At least thousand images were acquired for each pump flow setting (147 and 400 rpm) and for each of the six imaging regions. The raw particle images were processed using

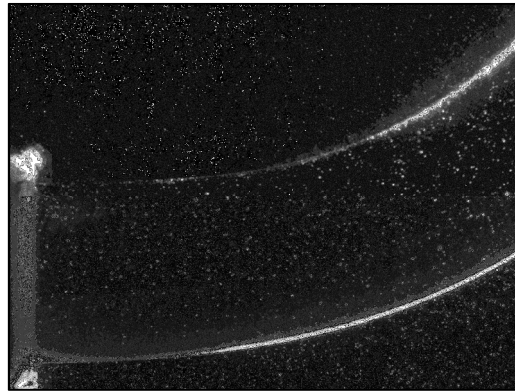
the PIVLAB2000 cross correlation software in Matlab (Han and Mungal, 2000) to produce a vector field containing 65 by 87 vectors at 0.42 mm vector spacing. These vector fields were later analyzed to obtain spatial and temporal information about the flow.

Stitching the six FOV's together to allow for an overall view of the bended flow is a crucial step to be considered here. Such a step can integrate data of different sections of the aorta into a single plot whether in the form of a vector field or contour levels. The process also provides a means of correlating shear stress – calculated throughout the walls – to a fully defined polar system  $(r, \theta)$  with an origin sitting on the center of the arch and zero-theta axis lying vertically downwards.

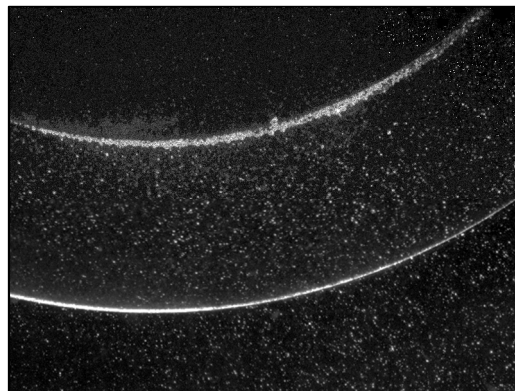
In **Figure 17** below, sample raw images of FOV1 and FOV2 are shown. In the case of FOV1, the camera was set to its zero-roll position prior to PIV. However, shifting to the next section of the arch, the camera was translated properly and rotated about its pivot for about  $37^\circ$  as read on an angular ruler (refer to figure 15). The read value is not sufficiently precise so another method was implemented to find a more precise camera roll angle; nonetheless, the read value was useful when used as a starting point in searching for the precise angle. The method has made use of the overlapping region which is a common region between two consecutive FOV's. Since static particles exist everywhere outside the aortic region, a particle sitting in the overlapping region was chosen randomly. A circular region having the randomly selected particle as its center was cut from both images. The two circular regions are identical, but there exists a rotational transformation between them. Circular region 2 was angularly cross-correlated with circular region 1. The cross-correlation function produces a correlation matrix containing a maximum, the value which



corresponds to the most precise rotational transformation. Hence, the roll angle of the camera is thus obtained. Similarly, the rest of the FOV's are stitched using the same method. **Figure 18** shows the stitched FOV's in a single picture.



(a)



(b)

**Figure 17** - Sample raw images of (a) FOV1 and (b) FOV2

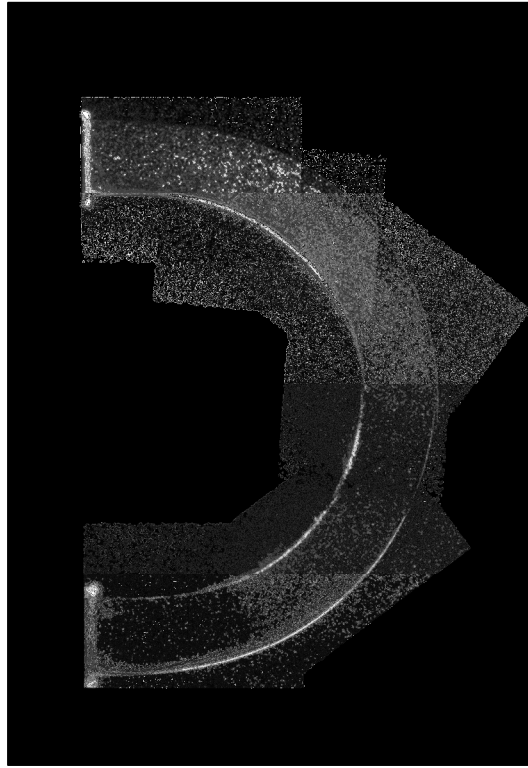


**Figure 18 - Stitched FOV's**

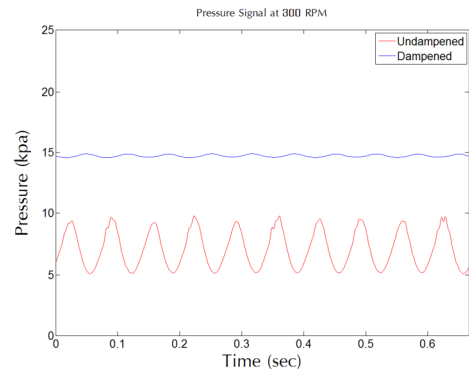
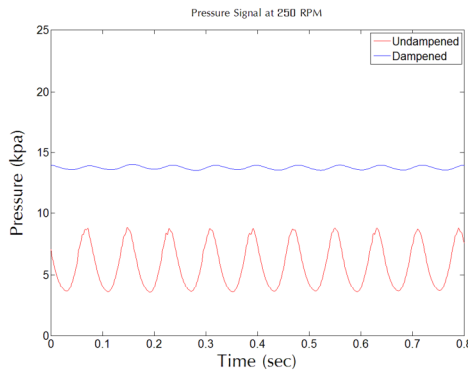
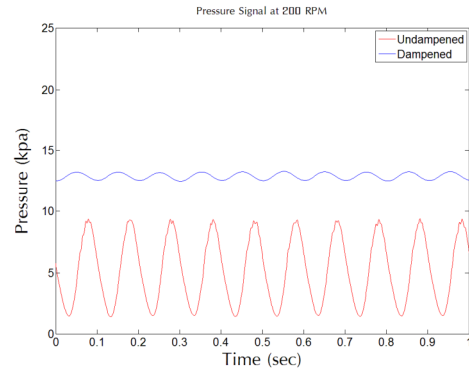
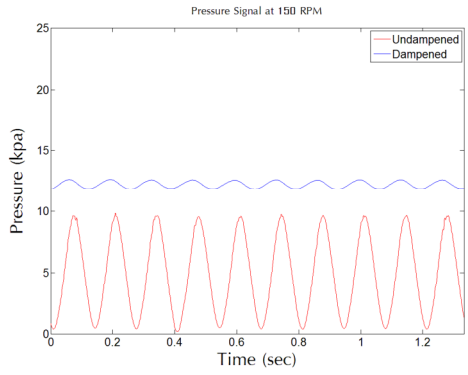
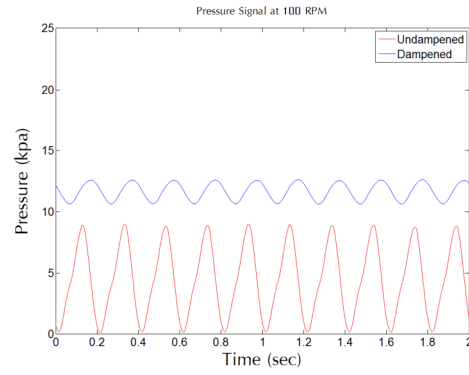
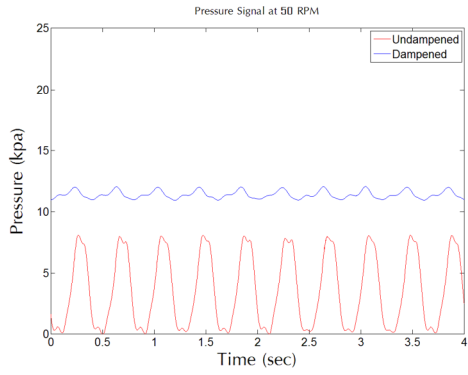
## CHAPTER IV

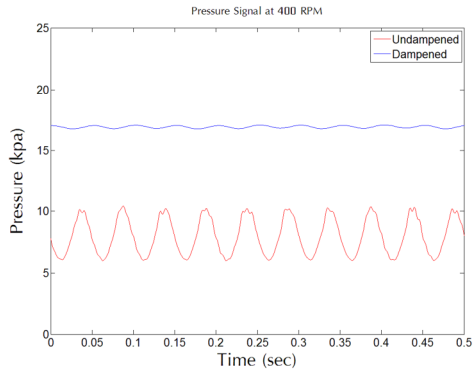
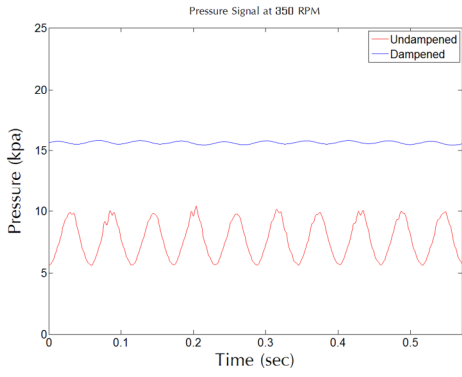
### PULSE DAMPENERS' EFFECTIVENESS

The installed pulse dampeners were effective at reducing the pulsatility of the system significantly. The ongoing study sheds light on the dampening effectiveness of the dampeners at different pulse frequencies and proves a useful functionality of them. A series of experiments were done on the present aortic flow loop system with the aim of extracting important characteristics of the flow with and without the pulse dampeners.

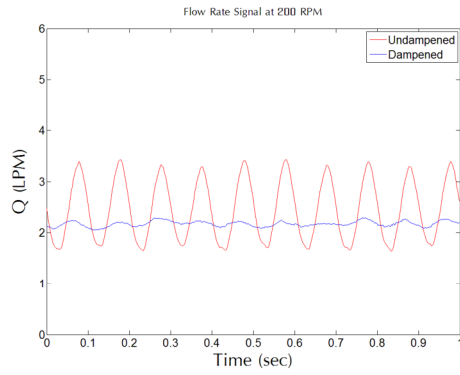
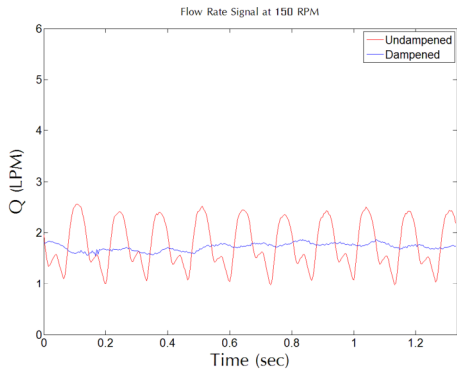
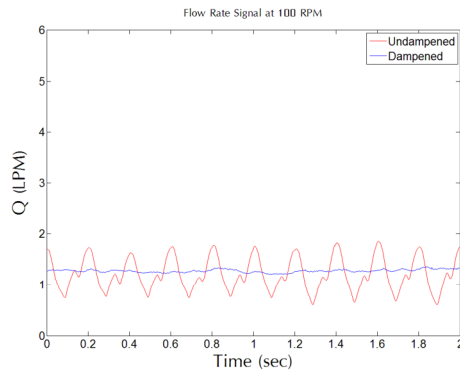
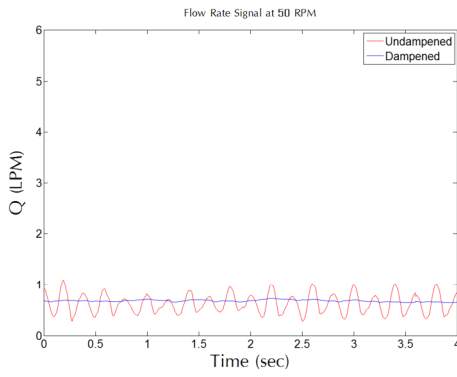
Flow rate and pressure are the two main quantities to be considered here. For the pressure, the provided pressure transducer at the aorta's outlet was precise enough to generate pressure data through time with a high sampling rate, specifically 1000 data points per second. For the flow rate, PIV was used to generate velocity fields at the inlet straight section, which are integrated spatially to produce flow rate through time. In Figures 17 and 18, pressure and flow rate signals are presented at different pump speeds, in rpm. Ten cycles of operation are presented in the figure at speeds ranging from 50 to 400 rpm. The peristaltic pump in use has an adjustable rpm option up to 400 rpm, with every revolution of the drum (rotor) involves 3 roller engagements on the tubing. This is equivalent to 3 pulses per revolution. Hence, the pump is said to operate up to 20 Hz (pulses per second). The pressure and flow rate signals are sinusoids with some shape imperfections in some cases. Flow rate signals, however, exhibit a higher degree of imperfections than pressure signals as can be seen in the figures. This shape imperfection could be thought of as a

system characteristic such as unsteady behavior, or a non-linear change of flow characteristic.





**Figure 19 - Pressure signals**



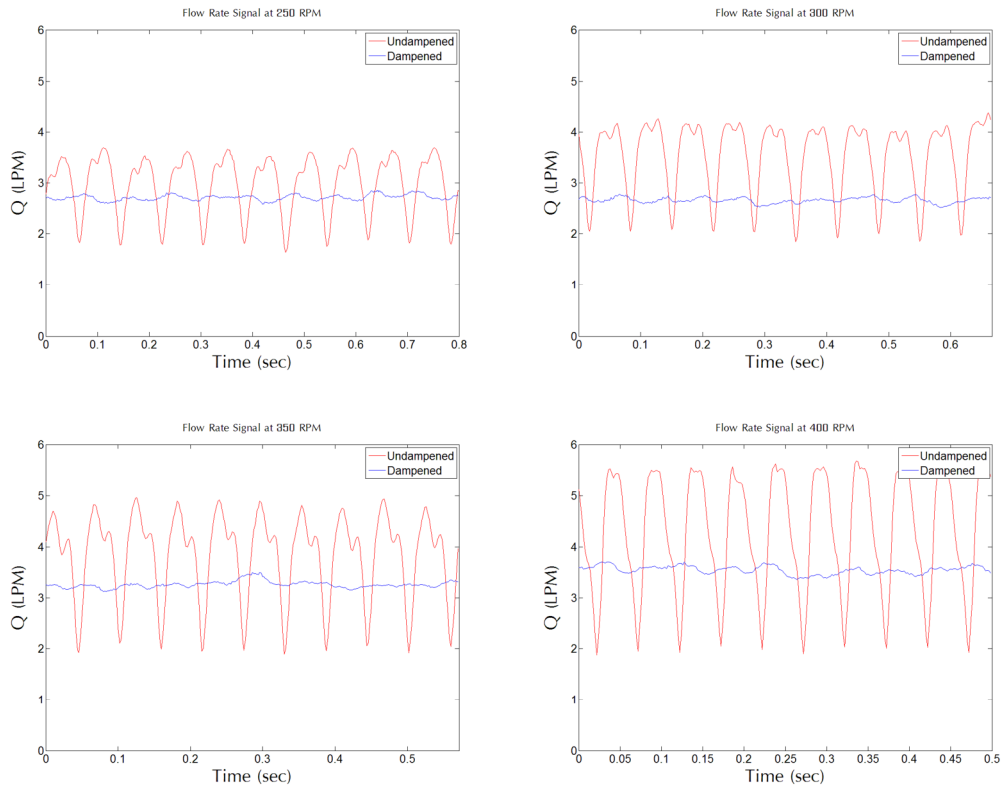


**Figure 20 – Flow rate signals**

To express a *dampening effectiveness* quantity of the pulse dampeners, an arbitrary formulation of a ratio for each of pressure and flow rate was formulated as follows:

$$e = \frac{\left(\frac{\sigma}{\mu}\right)_{UD} - \left(\frac{\sigma}{\mu}\right)_D}{\left(\frac{\sigma}{\mu}\right)_{UD}} \times 100$$

Where

- e*** Pulse dampeners' effectiveness ratio
- σ*** Standard variation of pressure/flow rate
- μ*** Mean of pressure/flow rate

And subscripts

***UD*** Undampened case

***D*** Dampened case

Plots of the pressure dampening effectiveness and flow rate dampening effectiveness are presented in Figures 21. Presented also in the same figures, a peak-to-peak ratio, which is another useful index of the effectiveness of the pulse dampeners. Peak-to-peak ratio is defined as:

$$r = \frac{(Y_{MAX} - Y_{MIN})_{UD} - (Y_{MAX} - Y_{MIN})_D}{(Y_{MAX} - Y_{MIN})_{UD}} \times 100$$

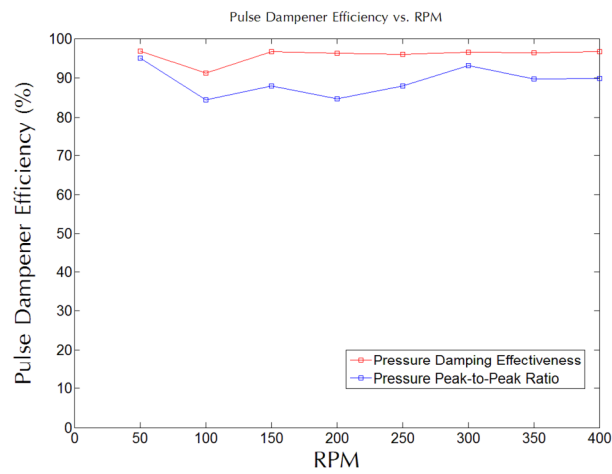
Where

***r*** Peak-to-peak ratio

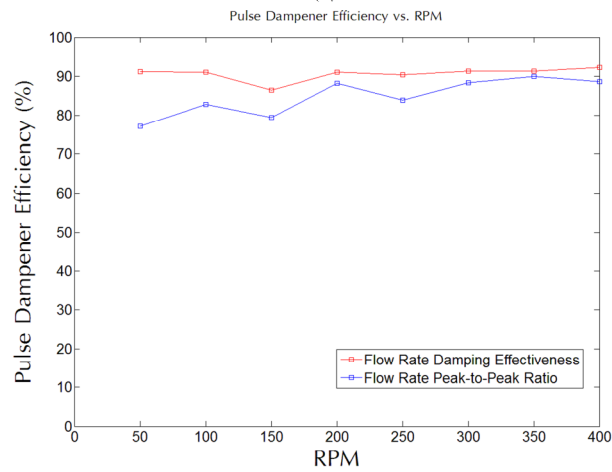
***Y*** Quantity of interest (Pressure/Flow rate)

The plotted ratios reveal high percentages for both quantities pressure and flow rate with a bit higher percentages for pressure. Pressure dampening effectiveness ratio has reached percentages of 95% at almost all frequencies; also flow rate dampening effectiveness ratio has reached percentages as high as 90% at almost all frequencies. The peak-to-peak ratio which expresses the pulse dampener's effectiveness from a different stance exhibits also fairly high percentages most of which lie in the vicinity of 85%. The present values of dampening effectiveness and peak-to-peak ratio are very promising, a fact

that contributes to isolating the system from undesirable sources of disturbance such as pulsatility. This finding has been a basis for the assumption of steady flow. Thus, in the results chapter, a temporal average PIV vector fields are to be implemented and no regard is to be made to the fine fluctuations in velocity and velocity driven quantities such as shear stress. This issue is explained in a clearer context in the next chapter.



(a)



(b)

Figure 21 - (a) Pressure dampening efficiency vs. time (b) Flow rate dampening efficiency vs. time



## CHAPTER V

### RESULTS

This chapter presents the PIV velocity patterns at the six specified fields of view (FOV). The FOV's are numbered from 1 through 6 starting from the inlet side (refer to figure 15). The running pump speeds, as previously mentioned, are 147 and 400 rpm; these are two modes of system operation mimicking rest and exercise states of an arterial blood flow. The velocity patterns to be presented are post-processed at a later stage to produce wall shear stress quantities at the inner and outer boundaries of the aortic arch. A thorough discussion of shear stress calculation is to be presented for consistency.

Figure 22 shows a sample PIV velocity field of FOV1 (inlet section) at 400 rpm. The presented velocity field is chosen at a random instant of time. Due to the dense figure, not all vectors were plotted; instead, vectors of even indices only were plotted with a suitable scale. Inner and outer boundaries were specified manually by choosing sufficient number of points on both of them. These points were then used to fit a 4<sup>th</sup> order polynomial function which precisely represented the actual boundaries. Originally, PIV yields displacement vectors in pixel units which require scaling and multiplying by the convenient factors. An accurate scale should be selected through defining a certain reference length (in mm) and its corresponding virtual length (in pixels). The reference length was chosen to be the aortic arch diameter at its inlet. The choice of the diameter at the inlet is convenient because an accurate measure of the actual diameter at the inlet is available. Measuring the virtual diameter is a straight forward method where pixels can be counted vertically from

the highest to the lowest point on the circumference. Then the scale is calculated as follows:

$$sc = \frac{L_{ref}}{L_{vir}} = \frac{D_{ref}}{D_{vir}} = \frac{13.5 \text{ mm}}{510 \text{ px}} = 0.0265 \text{ mm/px}$$

The inter-frame time is essential for attaining the required units of velocity (mm/s i.e.) as PIV generates displacements. In cinema PIV, the inter-frame time is the time interval between two successive shots of the camera, and this is defined as the reciprocal of the frame rate of the camera. Then, denoting the inter-frame time by  $dt$ :

$$dt = \frac{1}{fps}$$

Where

$fps$  Frame rate per second of the camera

Multiplying the PIV displacements by  $\left(\frac{sc}{dt}\right)$  yields the velocity vectors in mm/s. In

what follows, velocity and shear stress quantities will incorporate the defined scale.

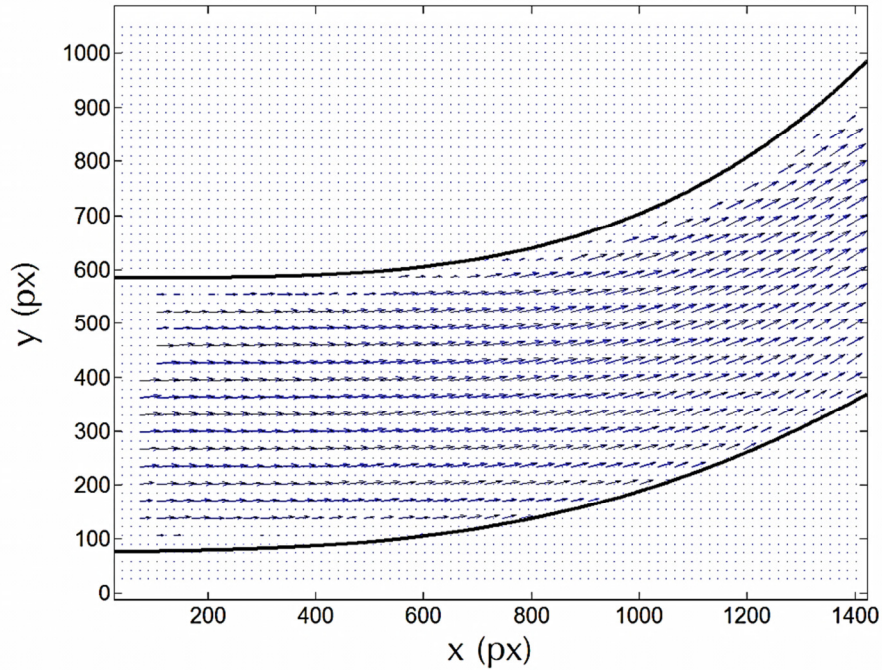


**Figure 22 - PIV velocity field at FOV1 at 400 rpm**

Figure 23 shows the average velocity signals at the inlet's cross section at 147 and 400 rpm for few cycles of operation. The dampening effectiveness of pulse dampeners can be observed in the signals. By referring to figure 23, it is worth mentioning that the employment of time-averaged velocity profiles throughout the aortic arch is reasonable in the present case. This is due to the fact that temporal velocity changes are fairly small. Though true the incident that temporal velocity changes have implications on the cell response, it is believed that the present case is quite untouched by those changes. This is justifiable when local shear stress levels are shown to be slightly varying with time. Figure 24 shows time-averaged velocity profiles at FOV1 for the two pump speeds, 147 and 400 rpm respectively with the scatter markers representing the time varying velocity profiles.

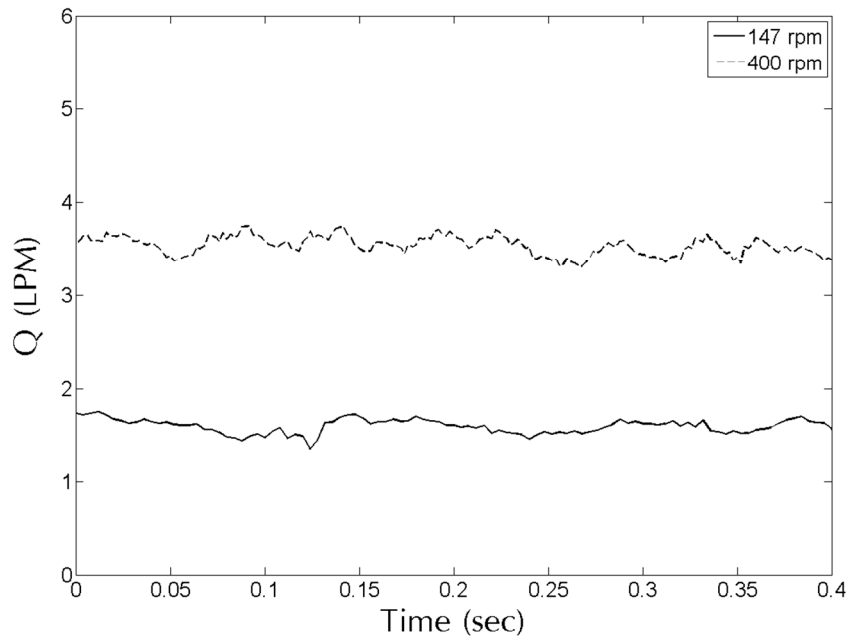
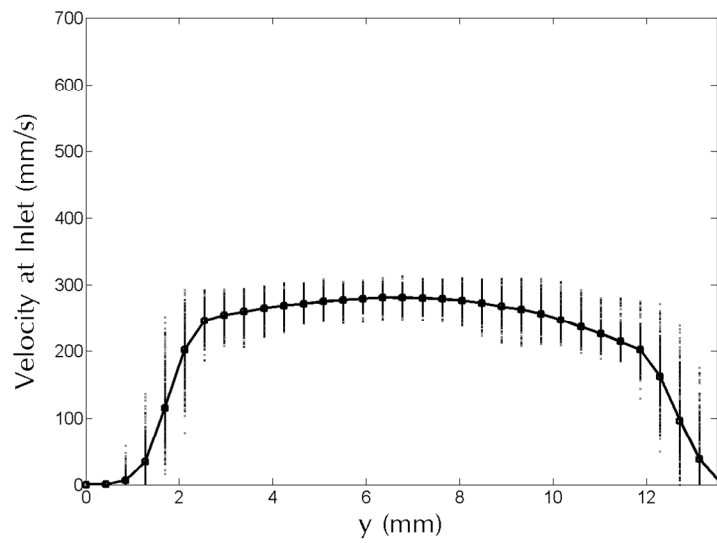
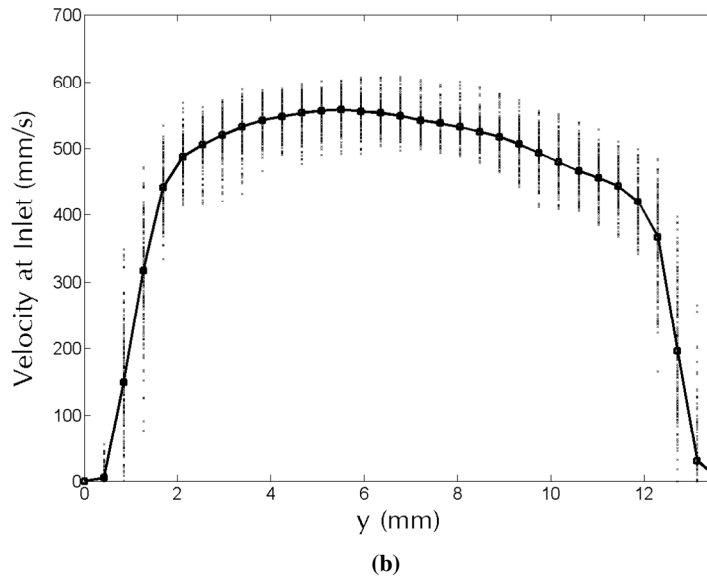


Figure 23 - Flow rate signal at 147 and 400 rpm



(a)



**Figure 24 - Time-averaged velocity profiles at the inlet for the two pump speeds (a) 147 and (b) 400 rpm**

The presented profiles in figure 24 are gradually increasing from zero at the walls to values as high as 280 mm/s and 550 mm/s for the two pump speeds 147 and 400 rpm respectively. There exists some degree of skewness in the right portion of the profiles, more prominent in the 400 rpm profile. For consistency, the right portion of the profile corresponds to the outer wall of the arch. The gradual increase of velocity at the boundaries seems to be linear, thus, the boundary regions were later represented by linear velocity functions. Figure 25 presents the time-averaged velocity fields and their corresponding contour of time-averaged velocity levels at 147 and 400 rpm for FOV1. The vectors of figure 26 are not drawn to scale because of their inconsistency with the domain; instead, they are scaled conveniently. A global view of the time-averaged velocity levels through the aortic arch is depicted in Figure 26 where the six sections are stitched according to the previously mentioned method. Figure 26 provides useful information about the behavior of

the flow. It shows how the flow decelerates near the inner wall as it proceeds through the arch. The deceleration action has started right at the point where the curvature of the inner wall starts. An appreciable deceleration can be observed at FOV2 where a stronger curvature of wall starts to appear. Accordingly, it is of great importance that FOV2 be examined in a more detailed framework. Figure 27 presents the time-averaged velocity fields and levels of FOV2 at 147 and 400 rpm. The 400 rpm case shows noticeable velocity gradients normal to the inner wall; this is represented by the fast transition of colors from red (high velocity) to green (low velocity).

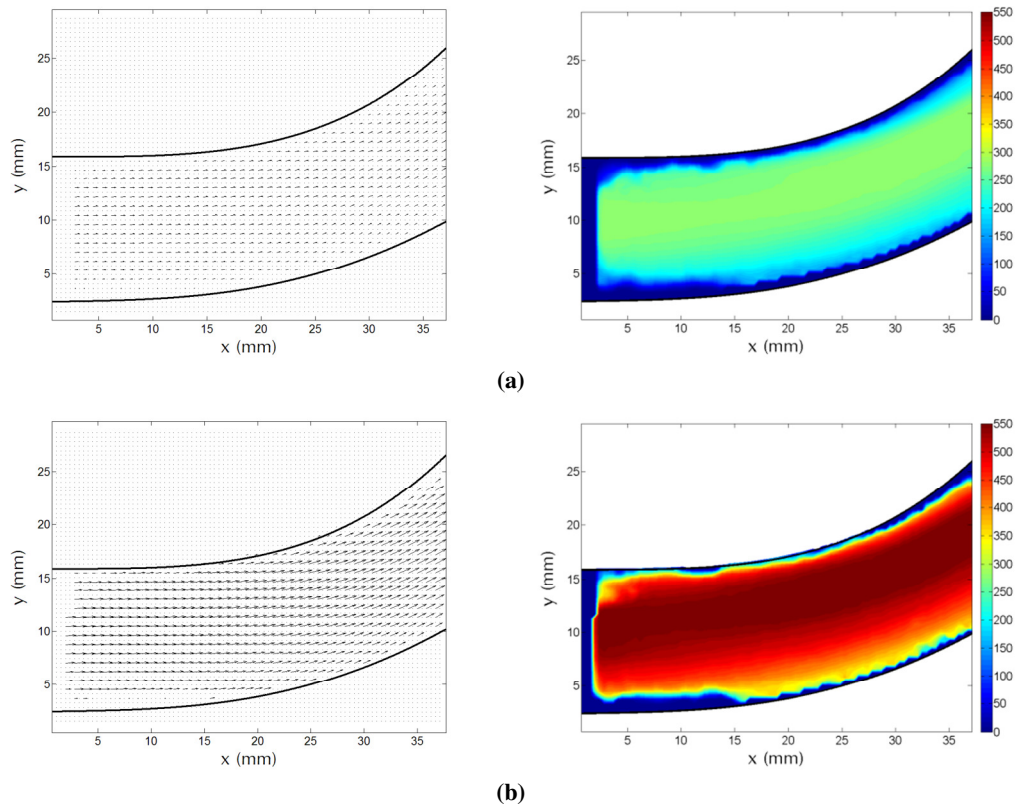
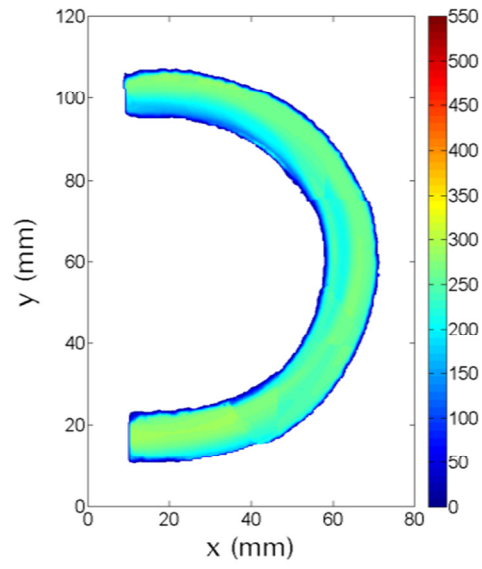
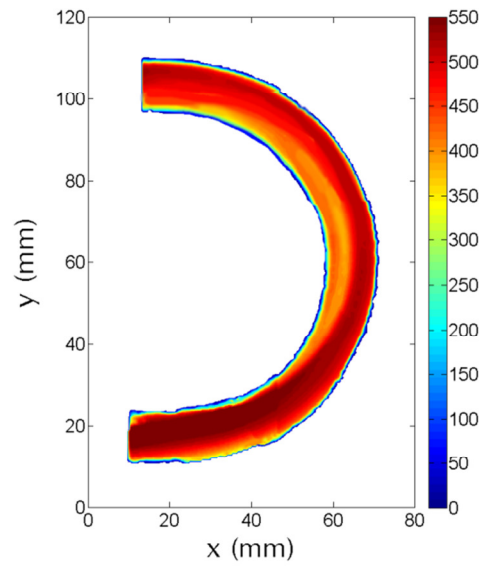


Figure 25 – Time-averaged velocity magnitude fields and levels at FOV1 at (a) 147 and (b) 400 rpm. Levels are in mm/s



(a)



(b)

**Figure 26 – Time-averaged velocity levels throughout the aortic arch at (a) 147 and (b) 400 rpm. Levels are in mm/s**

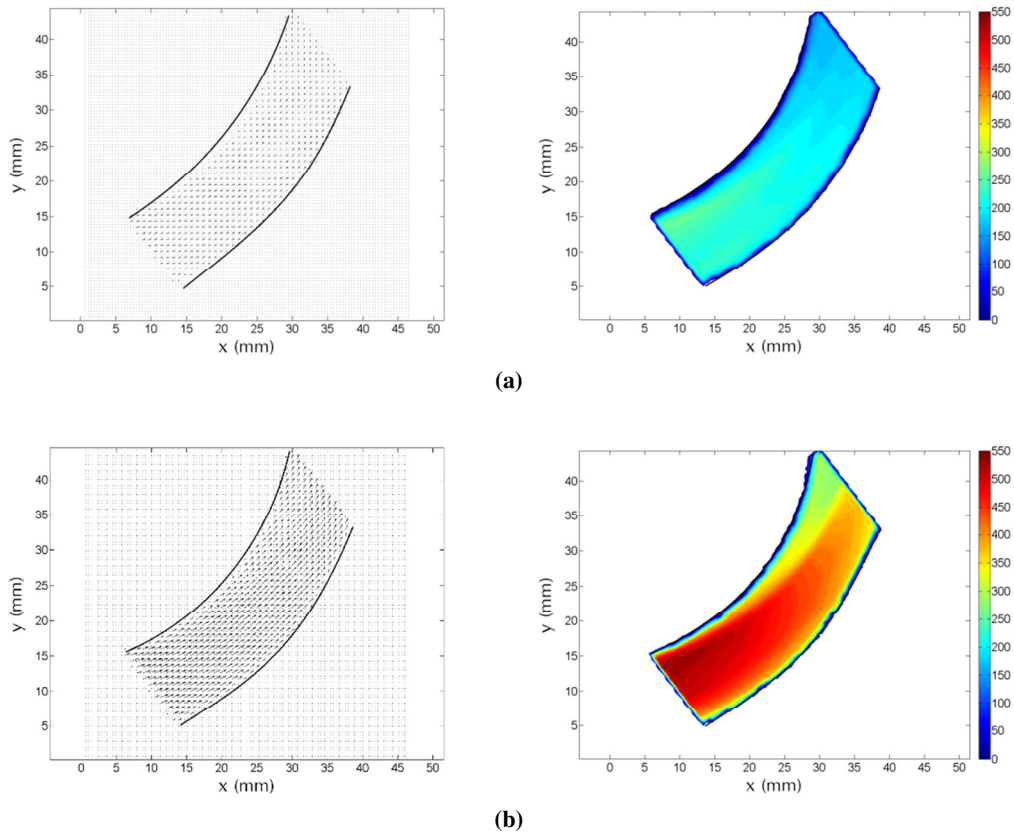


**Figure 27 – Time-averaged velocity fields and levels at FOV2 at (a) 147 and (b) 400 rpm. Levels are in mm/s**

As for wall shear stress calculations, a detailed approach will be presented here. The method starts by specifying, accurately, the boundary of the arch and choosing a point on the boundary at which the wall shear stress is to be calculated. In fact, many points will be chosen throughout the inner and outer walls. Wall shear stress calculations were done based on the velocity profiles obtained by PIV. Shear stress values are generated on several points on the inner and outer walls giving rise to useful shear stress distribution information along the walls. Shear stress ( $\tau$ ) is defined as:



$$\tau = \mu \left. \frac{\partial u}{\partial y} \right|_{y=0}$$

Where

$\mu$  Dynamic viscosity of the fluid

$u$  Velocity Component in the tangential direction

$y$  Normal distance from the wall

In **Figure 28**, a random region of the aortic arch is zoomed in. Shown in the figure, are groups of velocity vectors plotted starting from the wall and proceeding normally inwards. Since PIV vectors are evenly distributed – in rows and columns – it is not straight forward to get the vectors along a normal line. However, a *spline* interpolation was implemented to calculate the velocity vector at a given point based on the four neighboring vectors. It was proved through observing the full velocity profiles at many points through the wall that five points are most suitable for shear stress calculations. The nearly linear increase in the velocity profile in figure 24 was previously noted. Accordingly, a linear function at all points of interest on the wall has been calculated. **Figure 29** shows the aortic arch with an arbitrary polar system of origin O placed at the center of the arc. The angular span of the system starts from 0° at the inlet up to 180° at the outlet. Plenty of points are chosen on the inner and outer walls and shear stress is evaluated at them. For consistency,

the viscosity of the fluid at the specified *NaI* concentration and solution temperature is 0.00116 Pa.s.

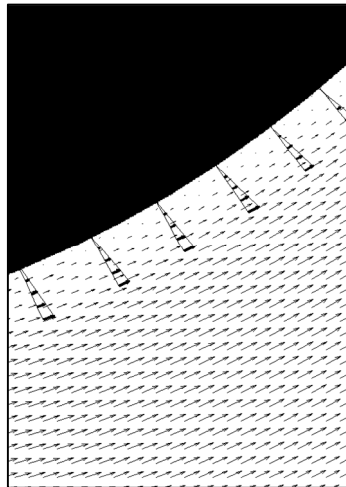


Figure 28 – A boundary region of the aortic arch showing sets of tangent vectors emerging from points on the boundary

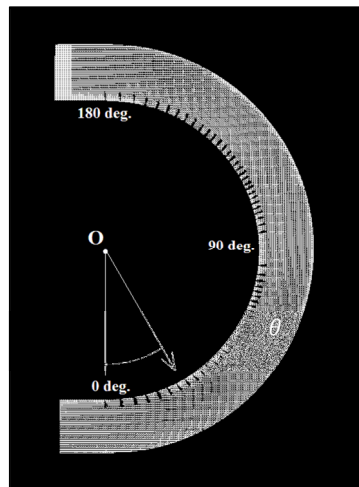
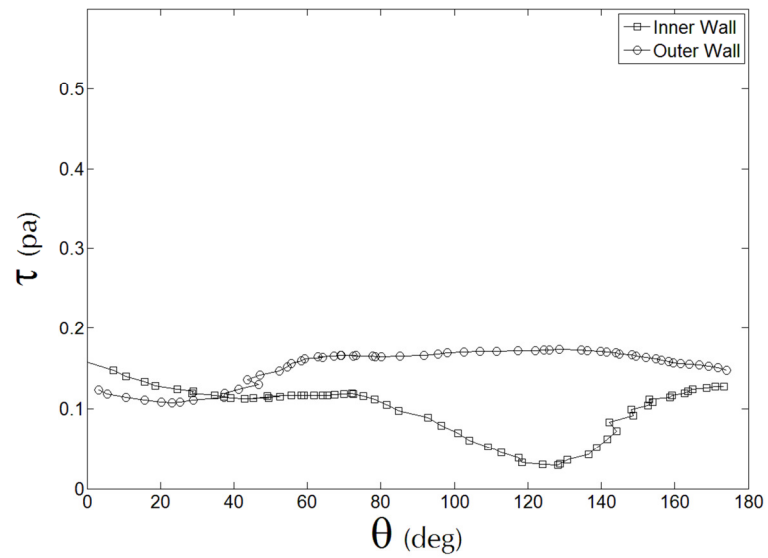
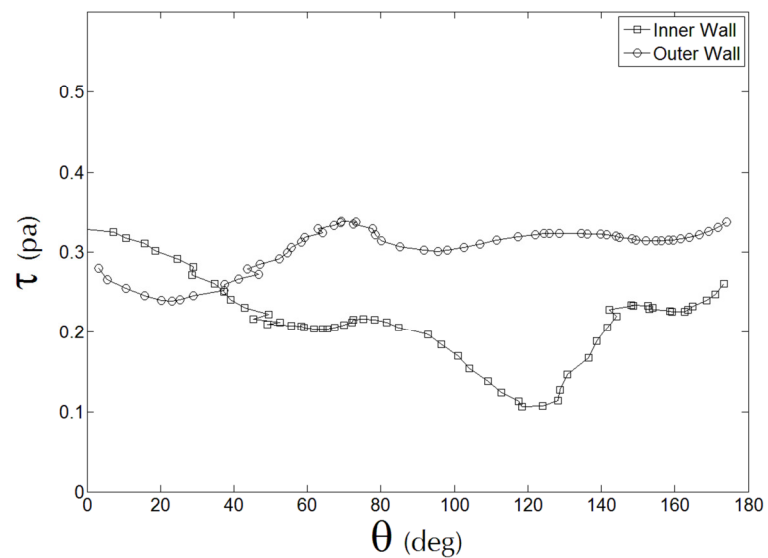


Figure 29 – A schematic showing the arch within the polar coordinate system ( $O, \theta$ )

**Figure 30** presents the shear stress ( $\tau$ ) in pa throughout the inner and outer walls of the aortic arch at the two pump speeds 147 and 400 rpm.



(a)



(b)

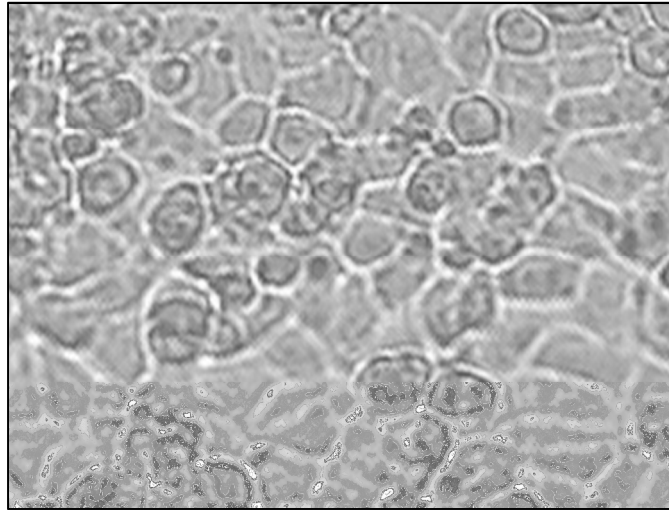
**Figure 30 - Shear Stress vs. theta along inner and outer walls at (a) 147 rpm and (b) 400 rpm**

Figure 30 shows smoothened shear stress values. A moving average was applied on the data to get rid of the small fluctuations; these are most likely due to the adding up of errors starting from the PIV velocity vectors which includes low-level inaccuracies due to averaging and also from the interpolation methods which include some sort of mathematical interpolation inaccuracies. This had required an efficient smoothing approach so a moving averaging filter is applied. At 147 rpm, following the inner wall shear stress curve, there's a gradual drop starting from  $0^\circ$  where shear stress value is 0.15 pa down to 0.04 pa at  $125^\circ$ . However, the outer wall shear stress curve slightly increases at the beginning where shear stress value is 0.15 pa till it reaches a quite steady level of 0.18 starting from  $60^\circ$ . Almost the same trends are observed in the 400 rpm shear stress curves; the inner wall shear stress drops gradually from 0.3 pa to 0.1 pa at  $120^\circ$  while the outer wall shear stress increases slightly from 0.3 pa till it reaches a steady level of 0.35 pa at  $60^\circ$ .

## CHAPTER VI

### BIOLOGICAL INVESTIGATIONS

Biological investigations have been done in the physiology lab. We investigated the different speed modes (low and high) on leptin expressions and ERK1/2 and cofilin phosphorylations. Endothelial cells were seeded on the interior wall of the lumen and cultured. The aortic arch was autoclaved prior to system operation in order to ensure sterility. Prior to operation also, it was crucial to test the ability of the cells to stick to the walls under flow conditions; a series of system operations were done at different durations 15, 60 and 120 minutes. The lumen walls were observed under a microscope at 40X and it was found that cells were still residing there, though not in the same initial density. **Figure 31** shows a magnified picture of cells after operation. On another occasion, the system was then operated at the two pump speeds 400 rpm and 50 rpm corresponding to high and low velocities. The duration of operation was 15 minutes; this is required to yield protein expression. Samples from the inner wall outer wall were collected for protein signaling study. A middle region of the wall between the upper and lower parts of the lumen was observed under the microscope. Two different alignments of the cells were recognized; the cells that exist in the upper part were shown to be uniformly aligned while those in the lower part were randomly aligned. This is presented in **Figure 32**.



**Figure 31 - Microscopic imaging of EC growth on the lumen of the aortic model 24 hours after seeding and under static conditions (40X)**

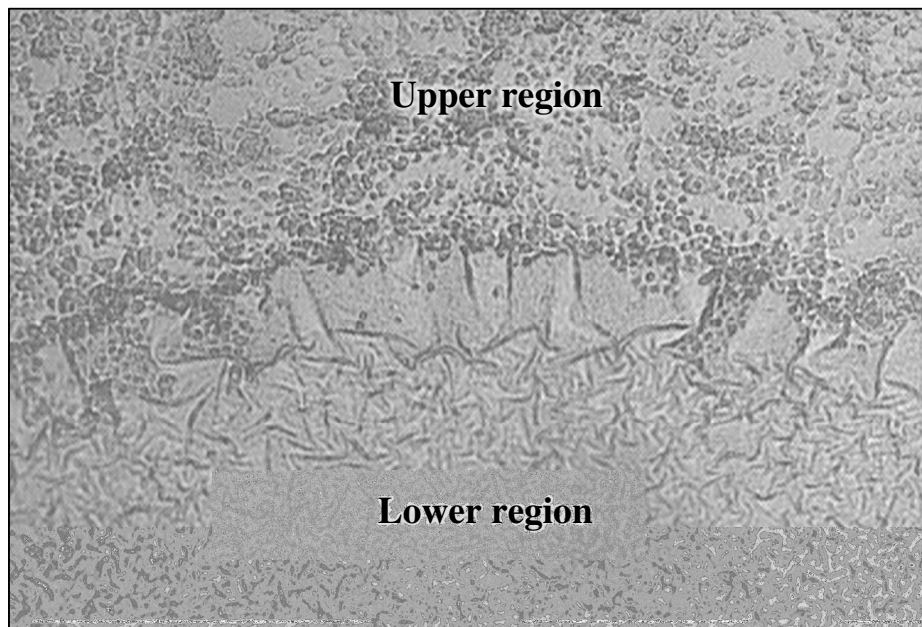
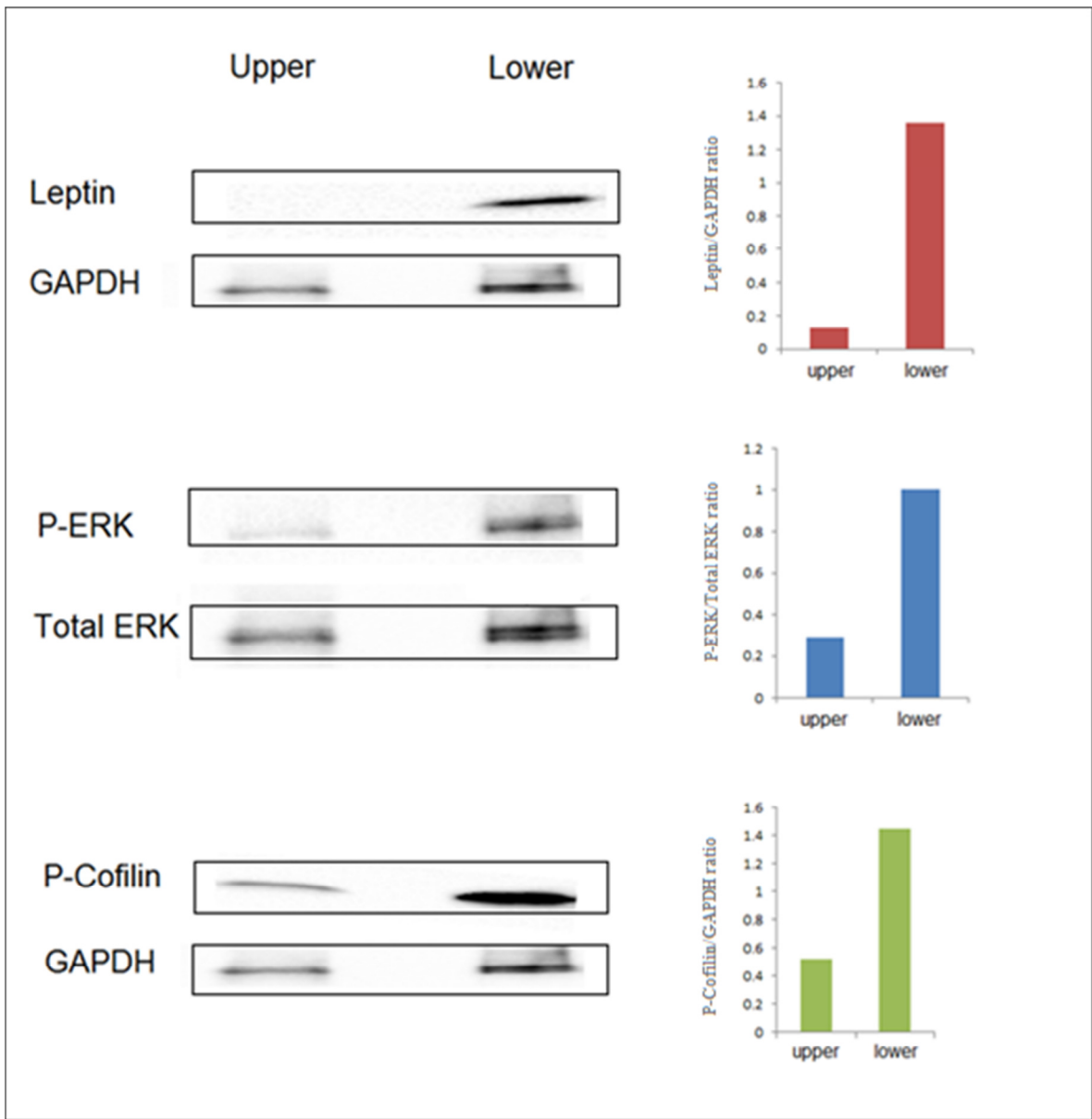


**Figure 32 - Upper and lower regions on the lumen show different EC alignments**

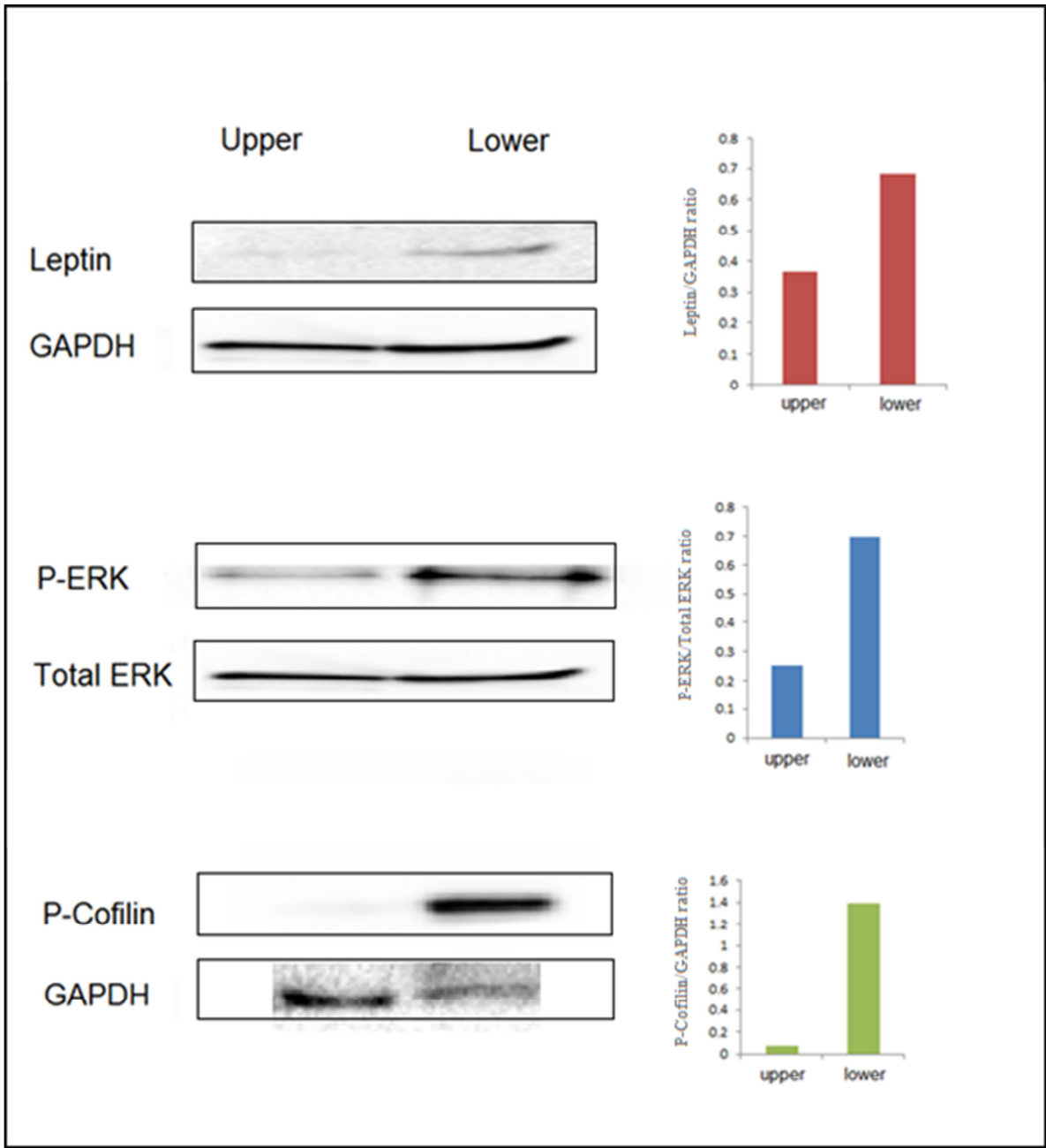
Protein expressions and phosphorylation were identified and quantified from the lower and upper regions. **Figure 33a and b** shows the effect of 50 and 400 rpm on the expression of leptin protein and ERK1/2 and cofilin phosphorylation

Protein expression and phosphorylation are conveniently normalized with GAPDH or total-ERK in the case of P-ERK, in order to apply reasonable comparison. Higher normalized quantities were noticed in the lower region than in the upper region. However, when comparing the normalized quantities of proteins from the lower region at 50 rpm versus those at 400 rpm, it is found that 50 rpm case exhibits higher quantities. This is presented in **Figure 34**.



(a)





(b)

Figure 33 - Protein expression and phosphorylation at (a) 50 rpm and (b) 400 rpm

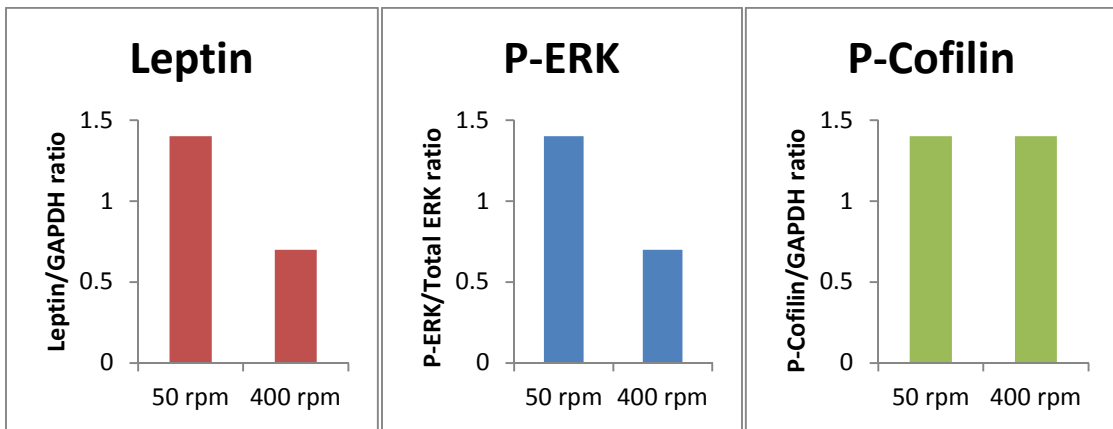
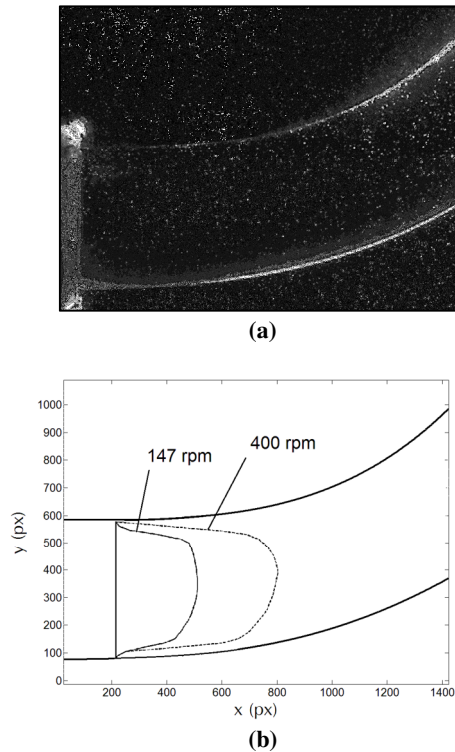


Figure 34 - Normalized protein quantities acquired from the lower region

## CHAPTER VII

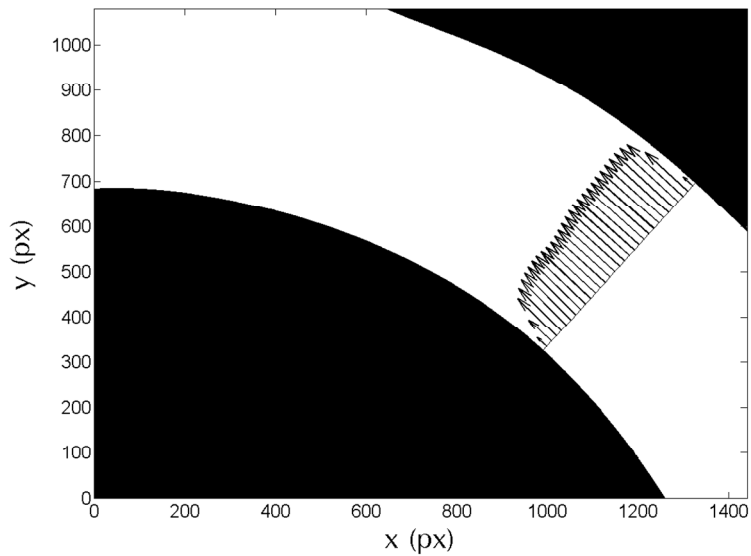
### DISCUSSION

The existing skewness in the velocity profiles shown in figure 24 is obviously due to the outer wall's curvature starting prior to that of the inner wall. This is illustrated in Figure 35. In fact, this is an imperfection of the aortic arch, believed to be an undesired effect of the tightening box which forces the elastic model to deform a little bit upon tightening.

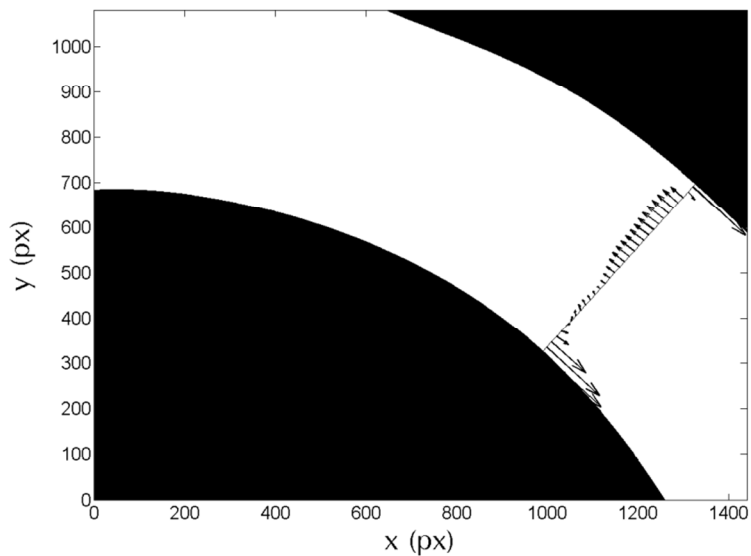


**Figure 35 – (a) A raw image of FOVI that shows how the lower (outer-radius) boundary is curved (b) Illustration of the velocity profiles skewness due to the outer wall curvature starting prior to that of the inner wall**

Shear stress variations along the inner and outer boundaries were expected to rely heavily on the acceleration and deceleration phenomena as shear stress is a function of the velocity gradients at the wall. From a fluid mechanics perspective, significant deceleration was expected at the inner walls and accordingly lower shear stresses (low velocity gradients) were expected. On the contrary, acceleration was expected at the outer wall and higher shear stresses were expected. In both cases, 147 and 400 rpm, the shear stress is dropping at the inner wall, but the 400 rpm case has shown a higher drop; this is because of the higher speed than that at 147 rpm relative to a 0 velocity at the walls – the well-known theoretical no-slip condition. The same reasoning for the shear stress at the outer wall; there's a higher increase of the outer wall shear stress at 400 rpm than that of 147 rpm case. The minimum shear stress point on the inner wall was shown to be that lying at  $\theta = 125^\circ$  for both cases. This is an interesting result where this angle can be thought of as a critical angle unaffected much by the speed of flow. A low shear stress means small velocity gradients at the wall and the latter is a direct consequence of flow deceleration. From another perspective, the velocity field could be presented in a differential framework. A certain methodology is to be made in order to view deceleration in a clearer framework. Re-circulation regions don't physically exist in the flow obviously because of the high convective behavior of the flow. Subtracting the local mean of velocity from a given velocity profile is one way to show a virtual re-circulating flow behavior. This is done for the 400 rpm case and shown in Figure 36.



(a)

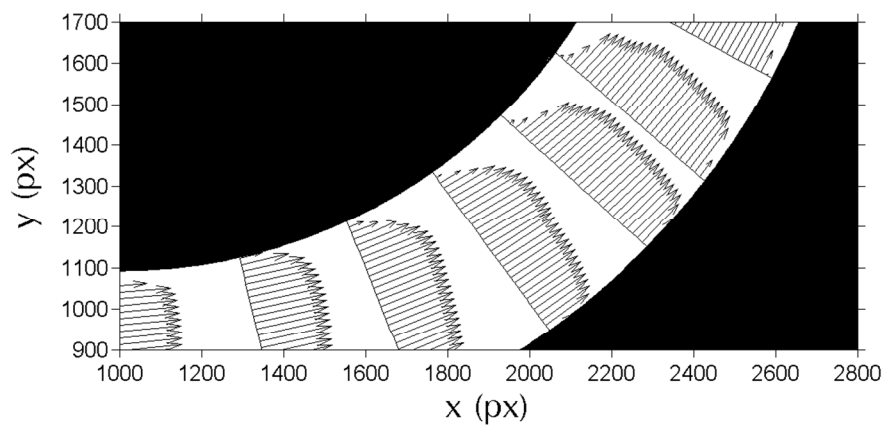


(b)

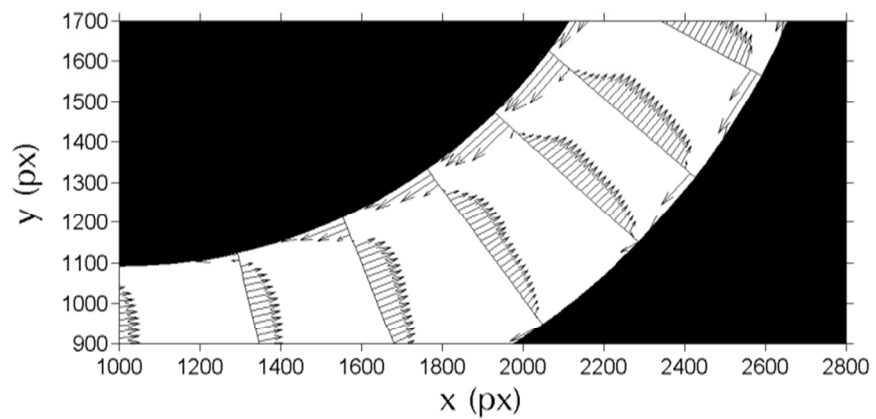
**Figure 36 - Velocity Profile at a given cross section of FOV5. (a) Actual velocity Profile (b) Velocity profile with mean subtracted**

In Figure 37, the same methodology is applied at the lower section of the aorta. The presented section is chosen because it is the region where an obvious increase in

deceleration is witnessed. The actual velocity profiles are shown in pixel units. The gradual increase of velocity from the inner wall normally inwards gets slower downstream. This is consistent with the velocity contour of figure 27-b where the deceleration is shown to be increasing downstream. Subtracting the local mean produces a better presentation of velocity profiles; this is shown in figure 37-b. Similarly, it is clear in figure 37-b the increase in the flow deceleration behavior at the inner boundary.



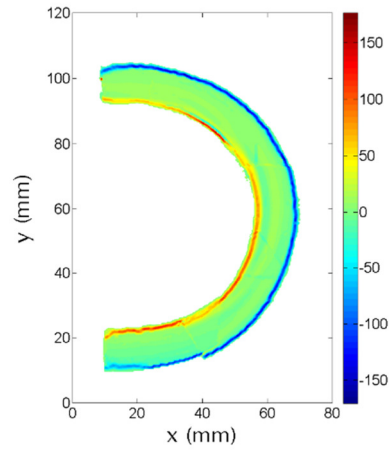
(a)



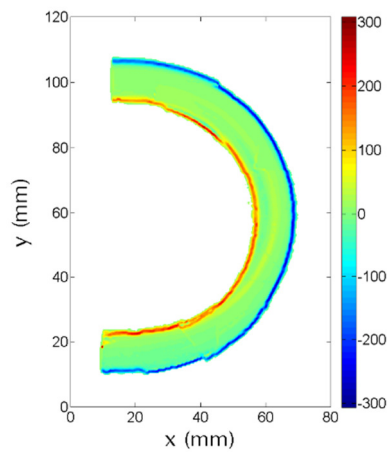
(b)

**Figure 37 – Velocity profiles at 400 rpm along a section of the aortic arch showing (a) actual velocity vectors and (b) modified velocity vectors by the subtraction of the local cross sectional mean of velocity**

An important parameter to be presented here is the vorticity level. The curl of the velocity field is calculated for the two cases 147 and 400 rpm. This is shown in **Figure 38**. A high vorticity level points to a high velocity gradient. Expectedly, figure 38 shows high vorticity levels at the boundaries.



(a)



(b)

**Figure 38 - Vorticity contour at (a) 147 rpm and (b) 400 rpm**

EC random alignment as well as high protein signaling from the lower aortic region point out to a low wall shear stress. This is in consistency with the calculated shear stress levels where they were shown to be lower at the inner wall than at the outer wall. Also, when the protein signals from the lower region at 50 rpm were compared to those at 400 rpm, higher quantities were observed in the 50 rpm case, and that's an additional piece of evidence which proves that the wall shear stress is strongly correlated to the protein expression.



## CHAPTER VIII

### CONCLUSION

The flow loop system had the ability to simulate typical flow conditions through an aortic bend, typical in dimensions. The main objective was characterizing the flow in the bend and calculating shear stress throughout its inner and outer walls. Two states of blood flow in aorta were simulated, rest and exercise states. These are mimicked by applying low and high flow rates. It was very important to ensure a suitable order of Reynolds number for both modes of operation in order to ensure consistent hemodynamic forcing. A sterile as well as optically clear medium was implemented by the convenient choice of the working fluid; *NaI* solution of a certain concentration and at a given temperature has yielded acceptable optical clarity in PIV imaging. The implemented pulse dampeners were very crucial in isolating the significant pulsatility produced by the peristaltic pump as can be seen in the pressure and flow signals as well as the effectiveness plots. The pulse dampeners were not totally killing the pulsations of the system, but still they were doing a great job in minimizing them. This finding has led to the assumption that time-variations were regarded as minimal and they were excluded from the reasoning. PIV velocity fields were generated throughout the whole aortic arch at two pump speeds, 147 rpm and 400 rpm; these are the low and high flow conditions of operation. The 147 rpm pump speed has driven an average flow rate of 1.8 LPM while the 400 rpm pump speed has driven 3.5 LPM. As for near-wall regions, where shear stress levels are to be calculated, velocity vectors were suitably characterizing the region as seen in the velocity profiles, so this has

opened a way for reliable shear stress estimates. Shear stress variations along the arch have shown low magnitudes at the inner wall as compared to the outer wall for both pump speeds. However, it was shown that the 147 rpm case has contributed in lower shear stress levels than those of the 400 rpm case due mainly to lower speeds. On the biology side, endothelial cells were seeded on the lumen and the system was made to operate. Protein signals were acquired from the lower and upper regions of the lumen and higher quantities of proteins were recognized in the lower region at both speeds 50 rpm and 400 rpm. Also when the proteins of the lower region were compared at 50 rpm versus those at 400 rpm it was found that they are higher in the 50 rpm case. This is in good consistency with the shear stress data which have shown low magnitudes at the inner wall (lower region) as compared to outer wall (upper region) and also in good consistency with the lower shear stress magnitudes found in the 50 rpm as compared to 400 rpm case. Given that, this research has proved through a series of fluid mechanics and biological investigations that hemodynamics experienced by blood flow have a major influence on the response of cells; when these hemodynamic forces' levels are low, bad proteins can exist in the vicinity due to the fact that blood is not able to remove them.

## REFERENCES

- [1] Thygesen K, Alpert JS, Jaffe AS, Simoons ML, Chaitment BR, White HD. Third universal definition of myocardial infarction. *Eur. Heart J.* 33, 2551–2567 (2012).
- [2] Steg PG, James SK, Atar D et al.; The Task Force on the management of ST-segment elevation acute myocardial infarction of the European Society of Cardiology. ESC Guidelines for the management of acute myocardial infarction in patients presenting with STsegment elevation. *Eur. Heart J.* 33, 2569–2619 (2012)
- [3] Lloyd-Jones, Donald, Robert J. Adams, Todd M. Brown, Mercedes Carnethon, Shifan Dai, Giovanni De Simone, T. Bruce Ferguson et al. "Heart disease and stroke statistics—2010 update A report from the American Heart Association." *Circulation* 121, no. 7 (2010): e46-e215.
- [4] Leal, J., Luengo-Fernández, R., Gray, A., Petersen, S., & Rayner, M. (2006). Economic burden of cardiovascular diseases in the enlarged European Union. *European heart journal*, 27(13), 1610-1619.
- [5] Ross, R. (1999). Atherosclerosis—an inflammatory disease. *New England journal of medicine*, 340(2), 1151-116.
- [6] Hansson, G. K. (2005). Inflammation, atherosclerosis, and coronary artery disease. *New England Journal of Medicine*, 352(16), 1685-1695.
- [7] Zeidan, A. et al. (2003) "Cholesterol Dependence of Vascular ERK1/2 Activation and Growth in Response to Stretch Role of Endothelin-1." *Arteriosclerosis, thrombosis, and vascular biology* 23.9 (2003): 1528-1534.
- [8] Cheng, C., Tempel, D., van Haperen, R., van der Baan, A., Grosveld, F., Daemen, M. J., et al. (2006). Atherosclerotic lesion size and vulnerability are determined by patterns of fluid shear stress. *Circulation*, 113(23), 2744-2753.
- [9] Chatzizisis, Y. S., Coskun, A. U., Jonas, M., Edelman, E. R., Feldman, C. L., & Stone, P. H. (2007). Role of endothelial shear stress in the natural history of coronary

atherosclerosis and vascular remodelingmolecular, cellular, and vascular behavior. *Journal of the American College of Cardiology*, 49(25), 2379-2393.

[10] Cheng, C., Tempel, D., van Haperen, R., van der Baan, A., Grosveld, F., Daemen, M. J., et al. (2006) Atherosclerotic lesion size and vulnerability are determined by patterns of fluid shear stress. *Circulation*, 113(23), 2744-2753.

[11] Hahn, C., & Schwartz, M. A. (2009). Mechanotransduction in vascular physiology and atherogenesis. *Nature Reviews Molecular Cell Biology*, 10(1), 53-62.

[12] Chiu, J. J., & Chien, S. (2011). Effects of disturbed flow on vascular endothelium: pathophysiological basis and clinical perspectives. *Physiological reviews*, 91(1), 327-387

[13] Walker, P G., Oweis, GF, and Watterson, KG. "Distribution of hepatic venous blood in the total cavo pulmonary connection: an in vitro study into the effects of connection geometry." *Journal of biomechanical engineering* 123.6, 2001: 558-564.

[14] Sakakibara, J., & Machida, N. (2012). Measurement of turbulent flow upstream and downstream of a circular pipe bend. *Physics of fluids*, 24, 041702.

[15] Bulusu, K. V., & Plesniak, M. W. (2013). Secondary flow morphologies due to model stent-induced perturbations in a 180° curved tube during systolic deceleration. *Experiments in Fluids*, 54(3), 1-13.

[16] W. R. Dean, Fluid Motion in a Curved Channel, *Proc. R. Soc. London, Ser. A* 121, 402-420 (1928).

[17] J. Eustice, *Proc. R. Soc. London Ser. A* 85 (1911) 119±131.

[18] Borsa JJ, Hoffer EK, Karmy-Jones R, Fontaine AB, Bloch RD, Yoon JK, So CR, Meissner MH, Demirer S., "Angiographic description of blunt traumatic injuries to the thoracic aorta with specific relevance to endograft repair, " *J Endovasc Ther.* 2002 Jun;9 Suppl 2:II84-91.

[19] Beller, Carsten J., et al. "Role of aortic root motion in the pathogenesis of aortic dissection." *Circulation* 109.6, 2004: 763-769.

[20] Ehrlich, Rita, Nisha S. Kheradiya, Diana M. Winston, Daniel B. Moore, Barbara Wirostko, and Alon Harris. "Age-related ocular vascular changes." *Graefe's Archive for Clinical and Experimental Ophthalmology* 247, no. 5 (2009): 583-591.

[21] O'Rourke, M. J., & McCullough, J. P. (2010). An investigation of the flow field within patient-specific models of an abdominal aortic aneurysm under steady inflow conditions. *Proceedings of the Institution of Mechanical Engineers. Part H, Journal of engineering in medicine*, 224(8), 971.

[22] Boutsianis, E., Guala, M., Olgac, U., Wildermuth, S., Hoyer, K., Ventikos, Y., & Poulikakos, D. (2009).

[23] CFD and PTV steady flow investigation in an anatomically accurate abdominal aortic aneurysm. *Journal of biomechanical engineering*, 131(1), 011008.

[24] Bai, K., Katz, J. (2014). On the refractive index of sodium iodide solutions for index matching in PIV. *Exp Fluids* 55:1704.

[25] Zaytsev ID, Aseyev MA (1992) Properties of aqueous solutions of electrolyte. *CRC Press*, Boca Raton